3.1. First publication

nanomaterials

Article

Transition Metal-Hyperdoped InP Semiconductors as Efficient Solar Absorber Materials

Gregorio García [1,2,*], Pablo Sánchez-Palencia [1,2], Pablo Palacios [1,3] and Perla Wahnón [1,2]

1 Instituto de Energía Solar, ETSI Telecomunicación, Universidad Politécnica de Madrid, Ciudad Universitaria, s/n, 28040 Madrid, Spain; p.sanchez-palencia@upm.es (P.S.-P.); pablo.palacios@upm.es (P.P.); perla@etsit.upm.es (P.W.)
2 Departamento de Tecnología Fotónica y Bioingeniería, ETSI Telecomunicación, Universidad Politécnica de Madrid, Ciudad Universitaria, s/n, 28040 Madrid, Spain
3 Departamento de Física aplicada a las Ingenierías Aeronáutica y Naval, ETSI Aeronáutica y del Espacio, Universidad Politécnica de Madrid, Pz. Cardenal Cisneros, 3, 28040 Madrid, Spain
* Correspondence: ggmoreno@etsit.upm.es

Received: 14 January 2020; Accepted: 4 February 2020; Published: 7 February 2020

Abstract: This work explores the possibility of increasing the photovoltaic efficiency of InP semiconductors through a hyperdoping process with transition metals (TM = Ti, V, Cr, Mn). To this end, we investigated the crystal structure, electronic band and optical absorption features of TM-hyperdoped InP (TM@InP), with the formula TMxIn1-xP (x = 0.03), by using accurate ab initio electronic structure calculations. The analysis of the electronic structure shows that TM 3d-orbitals induce new states in the host semiconductor bandgap, leading to improved absorption features that cover the whole range of the sunlight spectrum. The best results are obtained for Cr@InP, which is an excellent candidate as an in-gap band (IGB) absorber material. As a result, the sunlight absorption of the material is considerably improved through new sub-bandgap transitions across the IGB. Our results provide a systematic and overall perspective about the effects of transition metal hyperdoping into the exploitation of new semiconductors as potential key materials for photovoltaic applications.

Keywords: transition metal-hyperdoped; InP; photovoltaic; DFT; GW; in-gap band

1. Introduction

Despite the emergence of new renewable energy technologies, solar energy is still attracting a great deal of interest due to its abundant, clean and renewable characteristics. Even though silicon solar cells dominate the market share for photovoltaic (PV) technologies, there are considerable efforts to explore other semiconductor materials that could be used in photovoltaic devices [1,2]. To be an adequate solar cell material, a semiconductor would need to have a direct bandgap (to enhance light absorption and minimize nonradiative recombination). C.H. Henry estimated the thermodynamic limit of single-energy gap photovoltaic devices, pointing out that the conversion efficiency exhibits the highest values for bandgap values at ~1.10 and ~1.35 eV [3], being crystalline devices closer to the thermodynamic limit. T. Unold et al. assessed the relationship between the bandgap and the maximum obtainable open-circuit voltage (which is related to nonradiative recombination) [2,3], pointing out that crystalline materials such as GaAs and InP could reach the highest open-circuit voltage values (closer to the thermodynamic limit). Both InP and GaAs are III-V semiconductor materials with a direct bandgap (1.35 and 1.42 eV for InP and GaAs, respectively) [4] close to the optimum for solar energy conversion making them suitable candidates for solar cells. As matter of fact, energy conversion efficiencies of around 40% have been obtained for III–V semiconductors in multijunction tandem architecture at the laboratory scale [5]. GaAs has been widely studied despite the high toxicity of As atom [2,5–8].

Therefore, we have focused on InP, since this semiconductor achieves an optimal combination of bandgap width along with a high crystalline quality, to efficiently convert solar radiation into electrical energy. Unfortunately, even the most efficient InP solar cells have only reached efficiencies up to 22.1% [9–12]. Consequently, its efficiency as a solar cell material must be improved to reach up to (or even over) the theoretical maximum conversion efficiency ~ 33% based on the Shockley–Queisser (SQ) model [13].

Among the alternative designs that, theoretically, can exceed the SQ limit, large efforts have been made based on the in-gap band (IGB) concept. Those materials with an IGB (also known as an intermediate band) own a partially filled narrow band located between the valence and conduction bands (VB and CB, respectively) of the host semiconductor (see Figure 1). Thus, IGB materials could improve the conversion efficiency through a three-photon absorption process: from the VB to the CB, along with the absorption of two extra sub-bandgap photons (from the VB to the IGB and, from there, to the CB). This would lead to the creation of additional electron-hole pairs and a higher photocurrent without a decrease in the open-circuit voltage. Thus, the upper limit efficiency of an IGB solar cell could reach theoretical efficiencies of up to 63.1% [14–16]. In addition, the IGB must meet some additional requirements to improve its photovoltaic efficiency: (i) have its own small dispersion, without it being at a discreet level; (ii) be well isolated from the VB and CB to avoid thermalization between VB and CB; (iii) be partially filled to allow comparable rates between VB–IGB and IGB–CB transitions; (iv) have high concentrations of IGB states to produce high absorption coefficients for those sub-bandgap absorptions and avoid non-radiative recombination obtained through the formation of a highly delocalized energy band [14–16]. Among the major approaches considered in designing IGB materials, our group have extensively studied the formation of an IGB through the substitutional doping of some cations by a transition metal (TM) [17–36]. In this way, the *d*-orbitals of the TM might be located within the bandgap of the semiconductors, allowing for the formation of an isolated energy band, while the filling of the IGB can be finetuned through the adequate selection of the TM. To our knowledge, proposals for the creation of an IGB in InP semiconductor have not been suggested. Recently, J. Olea et al. synthetized GaP supersaturated with Ti by means of ion implantation, followed by pulsed-laser melting. The spectral photoconductivity measurements yielded an enhancement in the conductivity for energies below the bandgap of GaP, which were attributed to the presence of an IGB within the GaP bandgap [37]. The formation of an IGB in GaP hyperdoped with Ti was previously reported by our group using ab initio calculations [17,38,39].

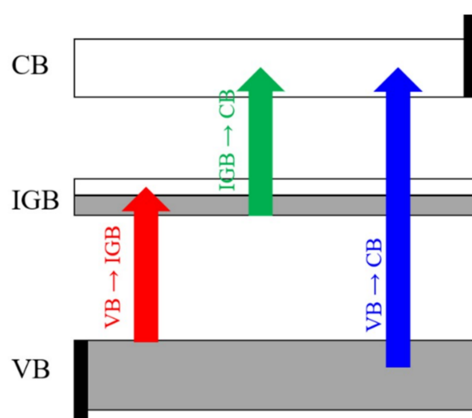

Figure 1. The IGB principle: photons of different energies promoted electrons VB to CB (VB→CB), as well as VB→IGB and IGB→CB, widening the photon range used.

The main goal of this paper is the study of the structural and electronic properties of several TM-hyperdoped InP (TM@InP) compounds in order to find new IGB materials with improved absorption features. Concretely, the selected TM were early 3*d*-block elements, whose ability to form

an IGB has been previously demonstrated [17,20,22,23,25,26,28–31,33–36,38–44]. Hence, in this work we investigate the structural, stability and electronic properties of several TM@InP (TM = Ti, V, Cr, Mn). It is well-known that standard density functional theory (DFT) methods are adequate to compute the structural and thermodynamic properties. The electronic properties of a semiconductor material are mainly characterized through the bandgap (E_g) value. Unfortunately, the commonly used DFT exchange–correlation functionals (such as the PBE one) dramatically underestimate the bandgap [45]. Aimed at providing an accurate description of the electronic structure and optical properties, DFT methods, along with the formalism proposed by Dudarev et al. (DFT+U) [46], were used. This method allows for a correct description of the band structure and density of states, but keeps the simplicity and excellent quality-to-cost ratio of standard DFT methods [47]. Although PBE+U formalism would be adequate for the native host material, such an approach has not been applied to in-gap band materials. Our previous works have demonstrated that the many-body perturbation theory in *GW* approximation (concretely G_0W_0 approach) [48], yields electronic structure information according to experimental data for other transition metal semiconductors with an in-gap band [24,34,35]. As a result, the electronic structure and optical absorption features were calculated using DFT+U, while G_0W_0 was used as benchmark method. We find that TM-hyperdoped InP semiconductors lead to an important absorption improvement, obtaining the most promising results for Cr@InP.

2. Computational Methodology

All calculations proposed here were performed using the Vienna ab initio simulation package (VASP) [49,50] within the framework of the DFT and many-body perturbation theory. The model system of InP was defined through a $2 \times 2 \times 2$ supercell containing 64 atoms. The crystal structure optimizations were performed using the PBEsol [51]. The Brillouin zone was sampled using an $8 \times 8 \times 8$ Γ-centered grid. The forces and total energies were converged to 0.01 eV Å^{-1}, 10^{-4} eV, respectively. The crystal structures of TM-hyperdoped InP (TM = Ti, V, Cr, Mn), with general formula $TM_xIn_{1-x}P$, were then built by replacing one In atom with a TM, which led to TM concentrations of x = 0.03, i.e., a concentration of 8.51×10^{22} cm^{-3}. Thus, the TM concentration studied was higher than the one required to yield high absorption coefficients for new sub-bandgap absorptions and to avoid non-radiative recombination [52].

In order to get over the bandgap underestimation of standard DFT methods, the electronic structure and optical absorption properties of InP and TM@InP were calculated through the DFT+U approach by using a PBE (PBE+U) exchange–correlation functional. This formalism was satisfactorily applied to other III–V semiconductor materials [53]. DFT+U formalism introduces a strong intra-atomic interaction in a Hartree–Fock-like manner, wherein the strength of the intra-atomic interactions is described by U (on-site Coulomb) and J (on-site exchange) parameters. According to the formalism proposed by Dudarev et al., only effective $U_{eff} = U - J$ parameters can account for the Coulomb interaction [46]. In this paper, the U_{eff} value was tuned to resemble the bandgap value of InP, calculated using a reference method (see below). Hence, several U_{eff} values (U_{eff} = 5, 8, 10, 15, 18 eV, see Figure S1) for the In atom were tested. As seen in Figure S1, a value of U_{eff} = 15 eV yielded an analogue bandgap than those calculated with the reference method, as well as in agreement with the experimental data [4]. We are aware that U should be chosen for each system separately. However, as seen below, U_{eff} = 15 eV is also adequate for TM@InP compounds with respect to the benchmark method.

The many-body perturbation theory in the *GW* approach [48] was used as reference method. Concretely, *GW* calculations were carried out to correct the PBE eigenvalues without further interactions, i.e., the G_0W_0 approach [48], wherein the calculation starts from the DFT eigenvalues and eigenfunctions to obtain many-body *GW* self-energy. It has been successfully proven that this method yields results that are in good agreement with the experimental results for IGB materials [34,35]. The G_0W_0 approach was carried out with a Γ-centered $4 \times 4 \times 4$ k-point to sample the Brillouin zone and 512 bands.

Finally, the optical properties were assessed through the absorption coefficient derived from the dielectric functions as, implemented in VASP code. The imaginary part of the dielectric function

was calculated as the sum of the independent transitions between Kohn–Sham states, without local field effects, while the real part was obtained from the imaginary part by means of the Kramers–Krönig relations. The imaginary part was decomposed as over independent transitions by using a home-modified version of the original OPTICS code developed by J. Furthmueller [50].

3. Results

3.1. Crystal Structure

InP semiconductor crystallized in a symmetry group of $F\text{-}43m\ \text{-}T_d^2$ (216) with a lattice constant of a = 5.873 Å [54]. In this structure, each In atom was surrounded by four P atoms in a tetrahedral environment and vice versa (see Figure 2). Table 1 gathers the lattice cell parameters and the most representative bond lengths for the optimized crystal structure (defined as a 2 × 2 × 2 supercell containing 64 atoms) of InP and TM@InP. As previously mentioned, in the case of the native host material, optimized structures led to lattice parameters and bond lengths that were in good agreement with the experimental data. The substitutional doping of In by a TM did not lead to important changes in the lattice cell of InP. For TM@InP compounds, TM atom was surrounded by a tetrahedron made up of four P atoms, with average bond lengths equal to d = 2.53 Å. This TM–P bond length was slightly lower (0.01 Å) compared with d(In-P) in the native compound. In addition, the six second nearest In atoms to the transition metal also defined a distorted octahedral void with a TM–TM distance equal to 4.16 Å. At the short range (i.e., in the vicinity of a TM atom, see Figure 2), In-P bond distances were barely increased with respect to the native compound (up to 0.02 Å), while no changes were found at the long range. Finally, P–P and In–In distances could be used as a measurement of the void distortion wherein TM was placed, compared with the In atom. In fact, the P–P and In–In bond lengths were 4.16 and 4.19 Å, respectively, at the short range (see d_1 (P–P) and d_1 (In–In) in Figure 2). However, P–P/In–In distances at the long range in TM@InP were slightly shorter/equal to P–P/In–In distances in the native compound. These variations were due to the smaller atomic radius of the TM compared with the In atom. Based on the results reported here, it can be concluded that the presence of TM atoms does not lead to an important crystal structure distortion in the host material.

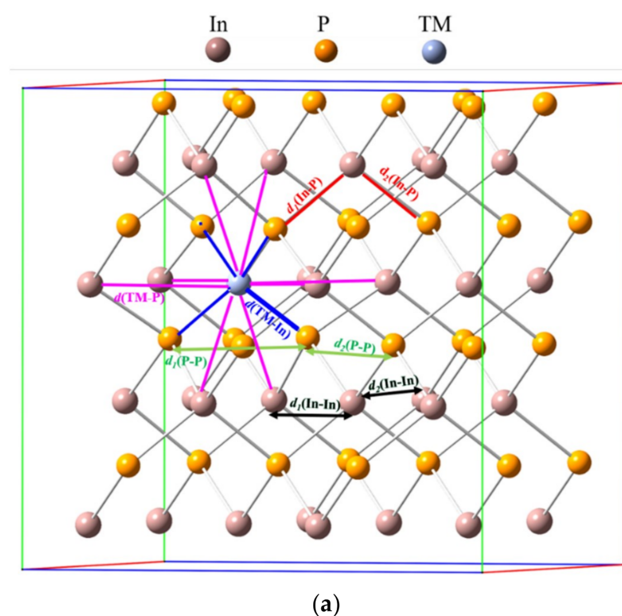

(**a**)

Figure 2. *Cont.*

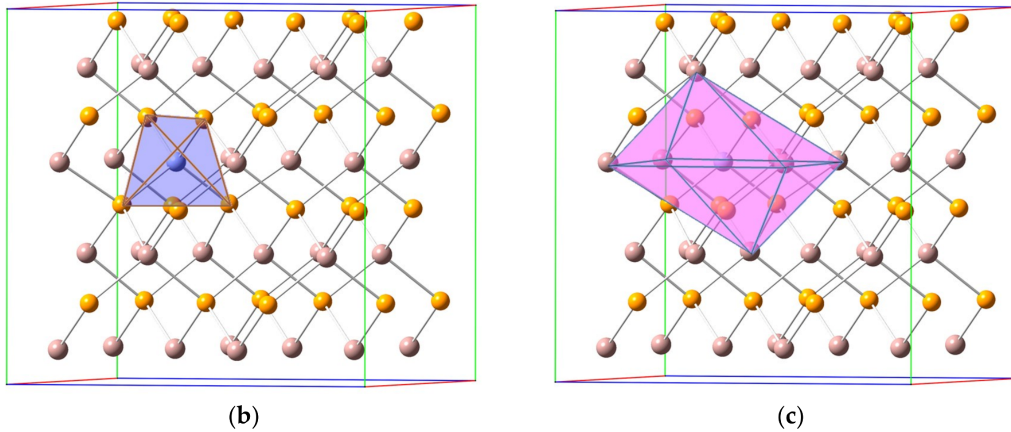

Figure 2. (**a**) Crystal structure of TM@InP along with main bond distances; (**b**) transition metals (TM) in a tetrahedral environment; (**c**) TM in an octahedral environment.

Table 1. Lattice parameters (a) and bond distances (d) obtained for optimized crystal structure of InP and TM@InP by using PBEsol functional along with experimental data of InP. For more details, see Figure 2. Units are in Angstroms (Å).

			TM@InP			
	InP [a]	**InP**	**TM = Ti**	**TM = V**	**TM = Cr**	**TM = Mn**
a	5.87	5.87	5.86	5.86	5.86	5.86
d(In-P)	2.54	2.54				
d_1(In-P) [b]			2.55	2.56	2.56	2.56
d_2(In-P) [b]			2.54	2.54	2.54	2.54
d(P–P)	4.15	4.15				
d_1(P–P) [b]			4.16	4.16	4.16	4.16
d_2(P–P) [b]			4.14	4.14	4.14	4.14
d(In–In) [b]	4.15	4.15				
d_1(In–In) [b]			4.19	4.19	4.19	4.19
d_2(In–In) [b]			4.15	4.15	4.15	4.15
d(TM–P)			2.53	2.53	2.53	2.53
d(TM–In)			4.14	4.14	4.14	4.14

[a] Experimental data taken from reference [54]. [b] The average values are collected for two kinds of bond lengths: (d_1) the closest ones to TM–P bond lengths and (d_2) the remaining ones.

3.2. Heat of Solution of TM@InP

The thermodynamic stability of the IGB materials studied in this paper were assessed through their solution enthalpies (heat of the solution, ΔH_s). For $TM_xIn_{1-x}P$, the heat of the solution can be defined as:

$$\Delta H_s = E^{TM@InP} - E^{InP} - \mu_{TM} - \mu_{In} \tag{1}$$

where $E^{TM@InP}$ and E^{InP} are the total energies of TM-hyperdoped InP compounds ($TM_xIn_{1-x}P$, x = 0.03) and the native host material (InP), respectively. μ_{TM} and μ_{In} are the chemical potential of the incorporated T(M atom (TM = Ti, V, Cr and Mn) and the In (replaced) atom, respectively. These chemical potentials are given by: $\mu_x = \mu_x{}^{Ref} + \Delta\mu_x$ (X = TM or In), where $\mu_x{}^{Ref}$ stands for the total energy of the X atom in its reference phase (see Table S1), and $\Delta\mu_x$ is the change in the chemical potential of the X atom when forming the compound of interest with respect to the chemical potential of its elemental phase. In addition, the stable phase field of InP implies that:

$$\Delta\mu_{In} \leq 0; \Delta\mu_P \leq 0 \tag{2}$$

$$\Delta\mu_{In} + \Delta\mu_P = \Delta H_f(InP) \tag{3}$$

where $\Delta H_f(InP)$ is the formation enthalpy of InP. Finally, the following constraints were also imposed: (i) P-rich conditions, which imply:

$$\Delta\mu_P = 0 \rightarrow \Delta\mu_{In} = \Delta H_f(InP) \tag{4}$$

(ii) the highest TM quantity was restricted by the formation of TMP as a competing phase. This secondary phase was defined with the same structure as InP, where all In atoms were replaced by a TM. Thus, both chemical potential of TM and P atoms must satisfy:

$$\Delta\mu_{TM} + \Delta\mu_P \leq \Delta H_f(TMP) \tag{5}$$

In all cases, the structure was relaxed at PBEsol level. For more details about the ΔH_s calculation, see reference [55]. The calculated heat of the solution is shown in Figure 3. The values for the heat of the solution lay between −22.08 eV (TM = Cr) and 14.33 eV (Ti). The calculated heat of the solution decreased from Ti (2 *d*-electrons) to Cr (*d*-5 electrons), while substitution with Mn (*d*-5 electrons) led to a slightly larger solution heat than those obtained for TM = Cr. As mentioned, the heat of the solution is negative for most TM-hyperdoped compounds (ΔH_s is positive only for TM = Ti), which means that substituting In with TM would be favored energetically. Positive ΔH_s values for Ti@InP would also be related to the atomic radius. It must be noted that, among selected TM, Ti atoms own the largest atomic radius, which would lead to a less-favored In replacement. In addition, the low positive heat of the solution can be overcome through adequate experimental conditions. In fact, positive heats of solution have been calculated for other IGB materials based on III-V semiconductor materials such as Mn@GaAs and Ti@GaP [39], which were experimentally synthesized [37,56].

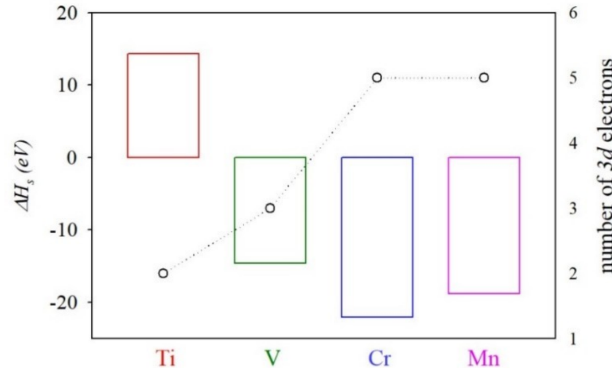

Figure 3. Calculated heat of solution (ΔH_s) of TM@InP compounds (TM = Ti, V, Cr, Mn) along with the number of *3d* electrons.

3.3. Electronic Band Structure

It is well known that sunlight absorption features are directly related to the electronic structure of the semiconductor material. Therefore, an accurate description of the electronic structure is needed. To overcome the bandgap underestimation obtained with common DFT methods, the electronic structure and optical absorption features of InP and TM@InP materials was calculated using PBE+*U*, while more accurate ab initio computational methods, such as many-body perturbation theory in the G_0W_0 approach, were used as reference methods (see above) [48]. The electronic structure and partial density of states (PDOS) of the native host semiconductor (InP), calculated with PBE+*U* (G_0W_0), are shown in Figure 4 (Figure S2). The results presented for InP were in agreement with experimental data [4]. The PBE+U (G_0W_0) results provided a direct bandgap of 1.37 eV (1.37 eV) at Γ point, which agreed with the experimental value (1.35 eV). As mentioned, both PBE+U and G_0W_0 approaches give similar

band structure and density of states patterns. A detailed inspection of the projected density of states (Figure 4) shows that the electronic structure near the valence band maximum (VBM) was mainly formed by participation of In-5*p* and P-3*p* states, while the conduction band minimum (CBM) was mainly due to In-5*s*, In-5*p* and P-3*p* states.

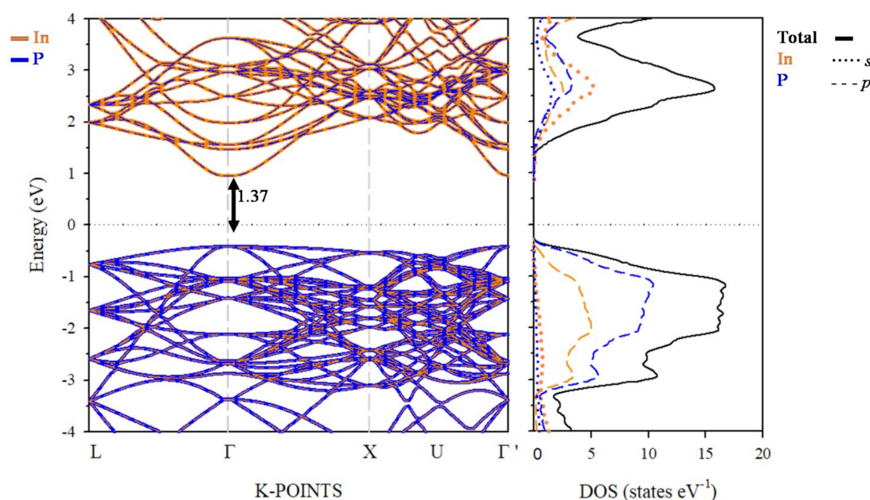

Figure 4. Projected electronic band structure (left) and density of states (DOS) (right) of InP calculated within PBE+U (U_{eff} = 15 eV) approach, along with main energy differences at Γ-point. The zero energy was set at the Fermi level (black dotted line). The spin-up and spin-down bands and DOS are not given separately, as both contributions were the same for the native InP material.

Figure 5 (Figures S3 and S4) shows the electronic band structure and PDOS of TM@InP calculated with PBE+U (G_0W_0). Once again, both PBE+U and G_0W_0 methods yielded a similar qualitative band structure and density of states patterns (even though calculated gaps with PBE+U were slightly underestimated with respect to G_0W_0). A detailed analysis of the PDOS showed that, upon In replacement by TM, the CB and VB did not change their nature significantly: the valence band maxima (VBM)was mostly due to the hybridization between In-5*p* and P-3*p* states, and the conduction band minimum (CBM) was due to In-5*s*, In-5*p* and P-3*p* states. For the spin-down channel, TM@InP compounds yielded a similar band structure pattern with a direct bandgap at Γ-point, which was opened to ~ 1.52 eV (1.63 eV), i.e., 0.15 eV (0.26 eV) with respect to InP.

For the spin-up component, when one In atom was substituted by TM, several new levels (green color in Figure 5) appeared between the edge bands of the host semiconductor (the blue and orange lines in Figure 5). Electronic structure changes upon TM hyperdoping could be described as a direct consequence of the crystal field created by P atoms around TM one. As discussed above, the TM atom was placed in a tetrahedral environment of P neighboring, with an TM–P bond length equal to 2.53 Å. In a high spin configuration, as surely was the case here, the interaction between the TM and P in a tetrahedral symmetry would cause a split of the TM-3*d* orbitals into a low-energy e_g doublet (due to d_{z^2} and $d_{x^2-y^2}$) and a high-energy t_{2g} triplet (d_{xy}, d_{xz} and d_{yz}), see Figure 6 [57]. This split was easily noted for all TM@InP compounds, except for TM = Ti. Starting from the Ti: $4s^2 3d^2$ and In: $5s^2 5p^1$ shell configurations, the e_g doublet would be semi-filled due to the extra electron, while t_{2g} orbitals would be empty. As seen in Figure 5, the E_{Fermi} penetrated in the first conduction band near the CBM (located at Γ-point), which was mainly due to Ti-3*d* orbitals. A detailed inspection of the PDOS showed that low-energy e_g doublet comprised two flat states on the Fermi level, whilst the first conduction bands were defined by the high-energy t_{2g} states (although they were also hybridized with higher conduction bands belonging to the InP). In short, the substitutional doping would lead to a bandgap increase up

to 1.49 eV at Γ-point (1.60 eV). For Ti@InP, VB–CB energy difference due to InP host semiconductor was opened to 1.88 eV (2.25 eV).

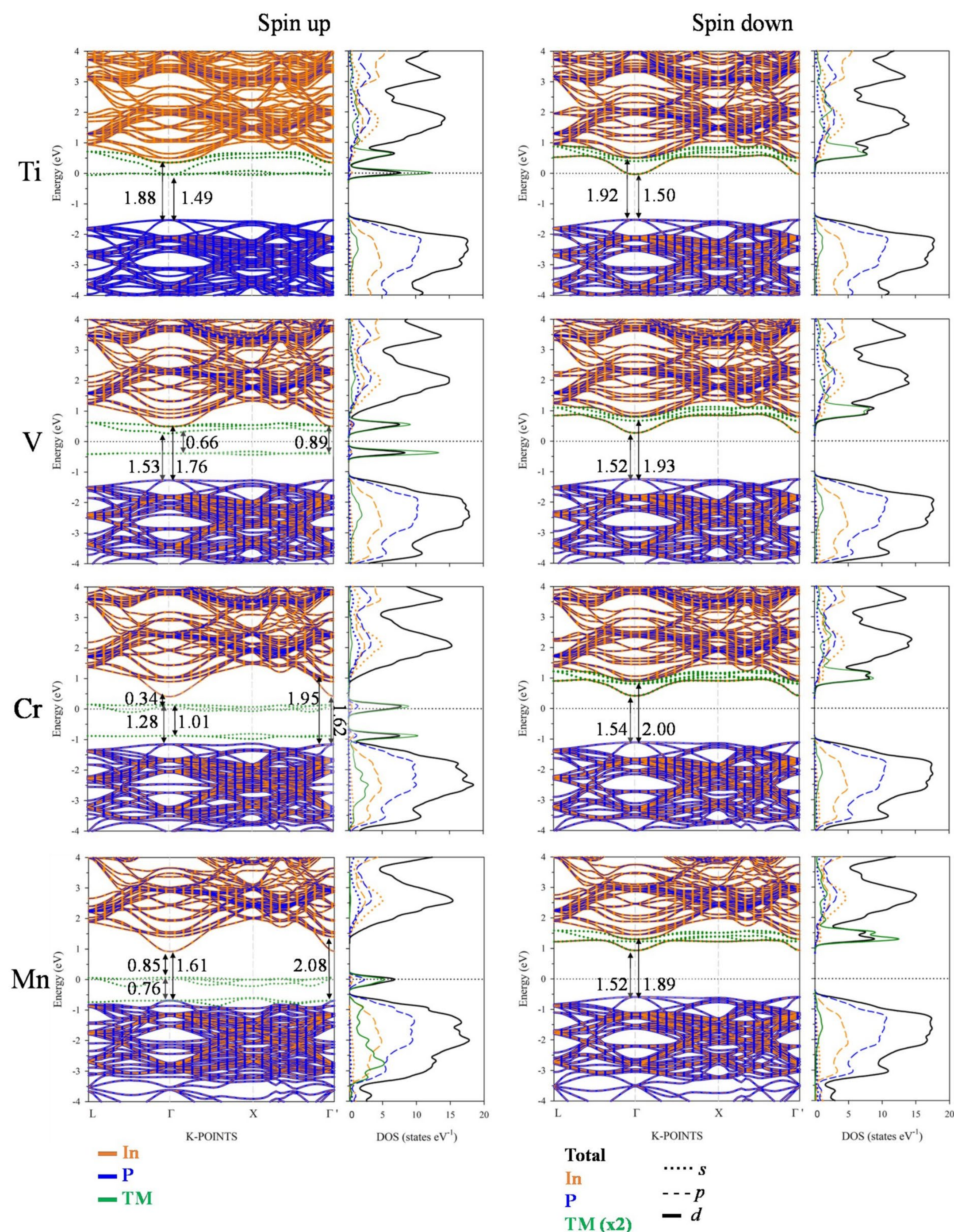

Figure 5. Projected electronic band structure (only the main atomic contribution was considered) and density of states of TM@InP calculated within PBE+*U* (U_{eff} = 15 eV) approach, along with main energy differences at Γ-point. The zero energy was set at the Fermi level (black dotted line).

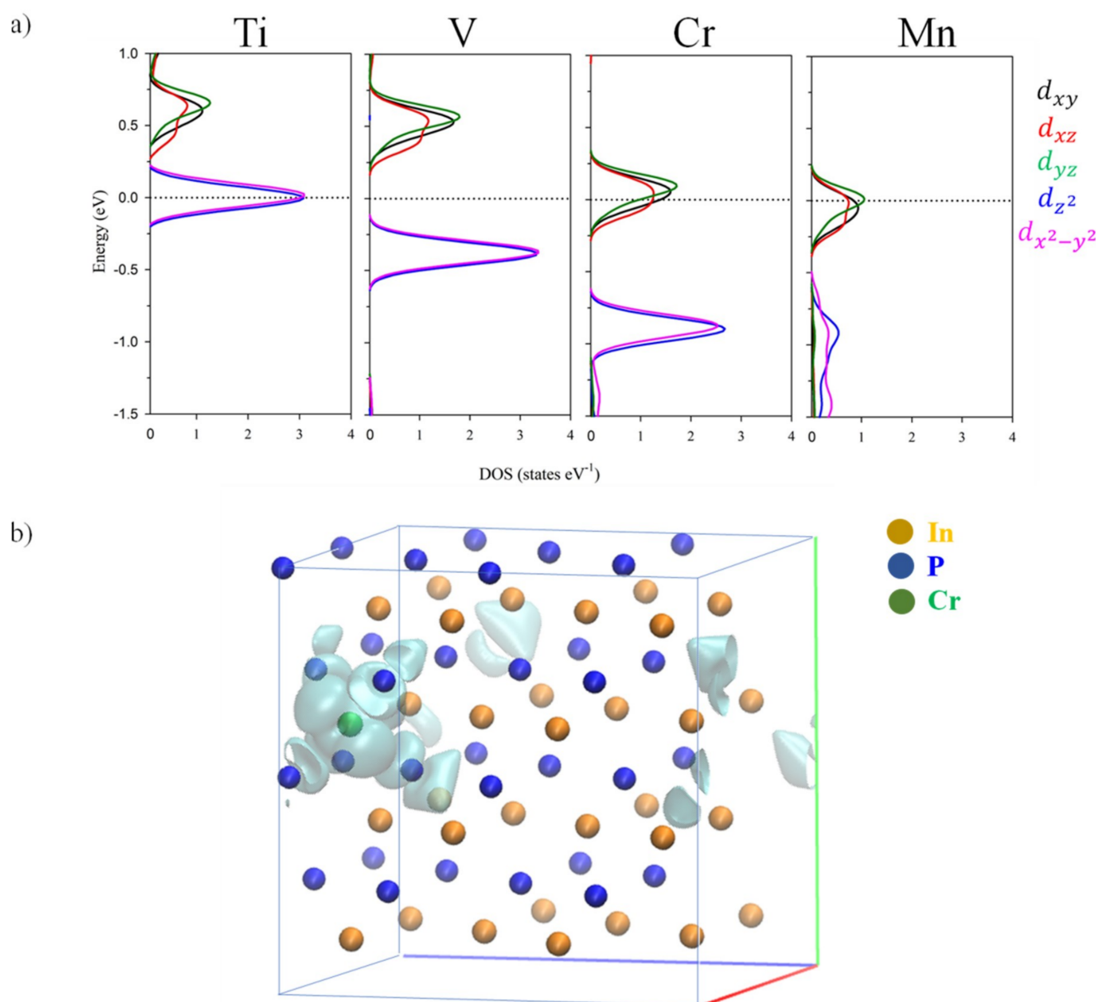

Figure 6. (**a**) Projected density of states of TM@InP showing the contribution of TM 3d-orbitals. The zero energy was set at the Fermi level (black dotted line); (**b**) the partial charge density of the intermediate band state for Cr@InP.

For TM = V ($4s^2 3d^3$), the low-energy e_g doublet (fully occupied with two electrons) was located at 0.39 eV (0.51 eV) below the E_{Fermi}. In addition, this level was well separated from the remaining valence band states belonging to the host InP semiconductor. The low-energy conduction bands were mainly due to t_{2g} manifold, which also contributed to the higher conduction bands. At Γ-point, the energy split between e_g and t_{2g} states was 0.66 eV (1.21 eV). Once again, the bandgap of the host semiconductor was importantly opened. Though the VB–CB energy difference for those bands belonging to the host semiconductor reached a value of 1.76 eV at Γ-point (2.02 eV), the bandgap of V@InP was notably smaller (0.66 eV), which corresponded to the energy split between e_g and t_{2g} states).

For Cr@InP (Cr: $4s^1 3d^5$ shell configuration), the low-energy e_g doublet was full of electrons, as well as close to the conduction band edge of the host material. In addition, Cr 3*d*-occupied states also contributed to lower conduction bands. As seen in Figure 5, there was an energy difference of 0.28 eV. The high-energy t_{2g} manifold met the requirements to be defined as IGB: (i) the band was partially filled (the Fermi level crossed it); (ii) the IGB was well isolated from both the CB (with an energy difference equal to 0.34 eV (0.49 eV) at Γ-point) and VB (the energy difference between the IGB and the VB belonging to InP host material e_g states was 1.28 eV (1.24 eV)); (iii) it had a small dispersion (with the largest bandwidth = 0.20 eV along the L-Γ and X-Γ′ directions), without being in a localized defect state.

As seen in Figure 6b, the wavefunction of the in-gap band state overlapped with the interacting orbitals of the neighboring atoms, which pointed to a non-localized defect state. The bandgap (VB–CB energy difference) of the host material increased to 1.62 eV at Γ-point (1.74 eV), as long as the presence of the IGB (due to t_{2g} states) also promoted new sub-bandgap optical absorptions. As previously pointed out, the upper-limit efficiency of an IGB solar cell could reach theoretical efficiencies up to 63.1%. Such upper limits are ruled by a host bandgap of 1.93 eV and a partial IGB which yields two sub-bandgaps of 0.70 and 1.23 eV, respectively [14–16]. However, the Cr@InP material yielded a host bandgap and sub-bandgap values that were far from those ideal values; a theoretical efficiency ~ 60% would be obtained based on its electronic structure [14–16]. This value still led to a considerable improvement with respect to the theoretical maximum conversion efficiency of ~ 33% based on the SQ model [13].

Mn@InP (Mn: $4s^2 3d^5$ shell configuration) yielded slightly different results depending on the computational method. According to the PBE+U approach, the low-energy e_g doublet (which was full) established the main contributions to the highest valence bands of this hyperdoped semiconductor, as well as important contributions to deeper valence bands (due to InP host material). Concerning t_{2g} states, this high-energy triplet could be defined as an IGB band. Considering the fact that the band was located on the Fermi level (it was partially filled with two electrons), it was well differentiated from the band edges (the energy difference between the IGB and the VB/CB was 0.76/0.81 eV (0.81/1.18 eV) at Γ-point) and it also owned a small dispersion (the largest bandwidth was 0.23 eV). Therefore, new optical sub-bandgap transitions across the IGB could be expected for Mn@InP. The main differences between the G_0W_0 and PBE+U methods were due to the dispersion of e_g states. In short, according to PBE+U, Mn semi-filled 3d orbitals (due to t_{2g} levels) were located on the Fermi energy level and were well differentiated from e_g states. Meanwhile, according to G_0W_0, both e_g and t_{2g} manifolds were completely split at Γ-points. Nonetheless, the dispersion of e_g states along L-Γ and Γ-X directions hindered the split between filled (e_g) and semi-filled (t_{2g}) Mn 3d levels.

3.4. Optical Absorption Features

Finally, the optical absorption features of InP and TM@InP compounds were studied through the dielectric function. From Figure 7, we can see that the measured absorption edge started at ~ 1.33 eV, which corresponds with the bandgap of the material (1.35 eV); then, the absorption spectrum showed some shoulders, and finally exponentially increased for the higher energies [58]. Although the approach that was used to compute the dielectric functions was only based on direct transitions, our results agreed well with the experimental data and reproduced the absorption behavior for InP. As matter of fact, InP is a well-known direct bandgap material. According to the DFT results, the absorption edge began at ~ 1.30 eV. The two peaks located at roughly 1.75 and 2.15 eV nicely reproduced the most abrupted shoulder in the experimental absorption spectrum at 1.75 and 2.15 eV.

Hyperdoping with TM led to an improvement in the absorption features below the bandgap of the InP. As seen in Figure 7, the absorption was extended up to 0.5 eV (as seen below, absorption peaks at lower energies did not contribute to the photocurrent generation), and there was an important increase in the photon absorption. The gained photon absorption was not only noted below the bandgap, but also for energies higher than the bandgap of InP. The highest absorption improvements were obtained for Cr@InP. Aimed at verifying the role of the TM in the absorption enhancements of TM@InP materials, the imaginary part of the dielectric functions was decomposed as a sum of the independent transitions (Figure 8). As discussed above, for the spin-down component, the main effect under TM hyperdoping was a bandgap decrease in VB and CB, mainly due to the host material, while 3d states were highly hybridized with the CB. Therefore, the total contribution from the spin-down channel was labeled as VB–CB. Except for Ti@InP, the absorption spectra of TM@InP (TM = V, Cr, Mn) was characterized by several peaks in the region below 1.50 eV. The first peak (0.20–0.25 eV) was due to the electronic transitions between the different states forming the high energy t_{2g} triplet (labeled as IGB-IGB in pink color), which was defined as IGB for TM = Cr and TM = Mn. Although these

low-energy transitions contributed to the overall absorption process, they were not directly related to the photocurrent generation of the device [43].

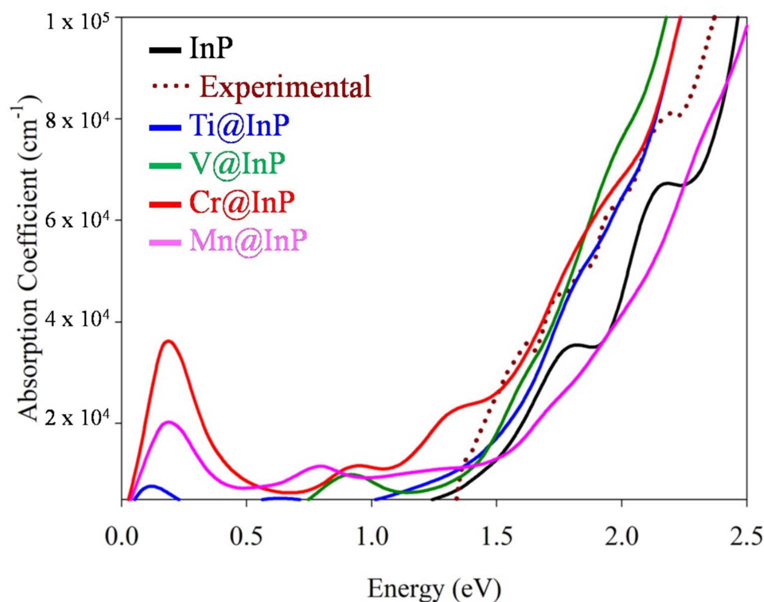

Figure 7. Absorption coefficients for InP and TM@InP (TM = Ti, V, Cr, Mn) compounds, along with experimental data for InP (taken from reference [58]).

Ti@InP and V@InP showed a bandgap decrease due to new transitions where 3*d* states were involved. Although both compounds owned 3*d* states in the forbidden gap of the material, none of them met the requirements to be an IGB. Therefore, the total absorption was due to the VB–CB transitions belonging to the host material (VB–CB transitions in blue), the VB–CB transitions where 3*d* states took part as donors (for simplicity, they are labeled as IGB–CB, in a red color) or acceptor levels (VB–IGB, labeled in a green color). For Ti@InP, the absorption edge considerably increased from ~ 1.50 eV due to VB–IGB transitions, which were related to the energy differences of 1.49 eV between the valence and e_g states (Figure 5). The small absorption peak at ~ 0.65 eV mainly originated from IGB–CB (in concordance with the energy difference ~ 0.70 eV that was measured for Ti@InP at L-point and along X-Γ′ directions). For V@InP, the dielectric function gradually increased from 0.70 eV due to VB–IGB, while VB–CB transitions were mainly contributors from 1.50 eV. Mn@InP was the only system that yielded different results depending on the applied method (PBE+*U* or G_0W_0), above the split energy between e_g and t_{2g} states and, consequently, on the formation of an IGB. The enhancement of the absorption between 0.50 eV and 1.50 was due to IGB–CB (it started to appear at 0.50 eV, reaching the highest intensity at 0.90 eV) and VB–IGB transitions (which began at 0.70 eV, reaching the highest intensity at 0.85 eV), respectively. For energies larger than 1.50 eV, VB–CB transitions were the main contributors to the total absorption. It should be noted that, based on the G_0W_0 electronic structure, that VB–IGB transitions would barely contribute to the total dielectric function, decreasing the gained absorption.

Among the different hyperdoped InP materials, Cr@InP provided the best improvement of the gained photo-absorption. As seen in Figures 7 and 8, the absorption was extended below the bandgap up to 0.75 eV due to VB–IGB transitions, which reached the highest intensity at 1.35 eV. There was also a small IGB–CB contribution (the highest intensity was at 1.15 eV). Both VB–IGB and IGB–CB transitions were the main contributors to the absorption of energy ~ 1.75 eV, which corresponded to the electronic transitions between the deeper valence bands and the IGB, and between the IGB and the higher conduction bands. Regarding the VB–CB transitions, they were the main contributors to

absorption energies over 2.00 eV. In short, all TM@InP compounds studied in this paper provided an absorption improvement through new transitions, due to the TM 3*d* states located in the forbidden gap of the host material. However, the presence of an IGB with the adequate properties for Cr@InP yielded the highest absorption improvement in the whole range of energies with photovoltaic applications.

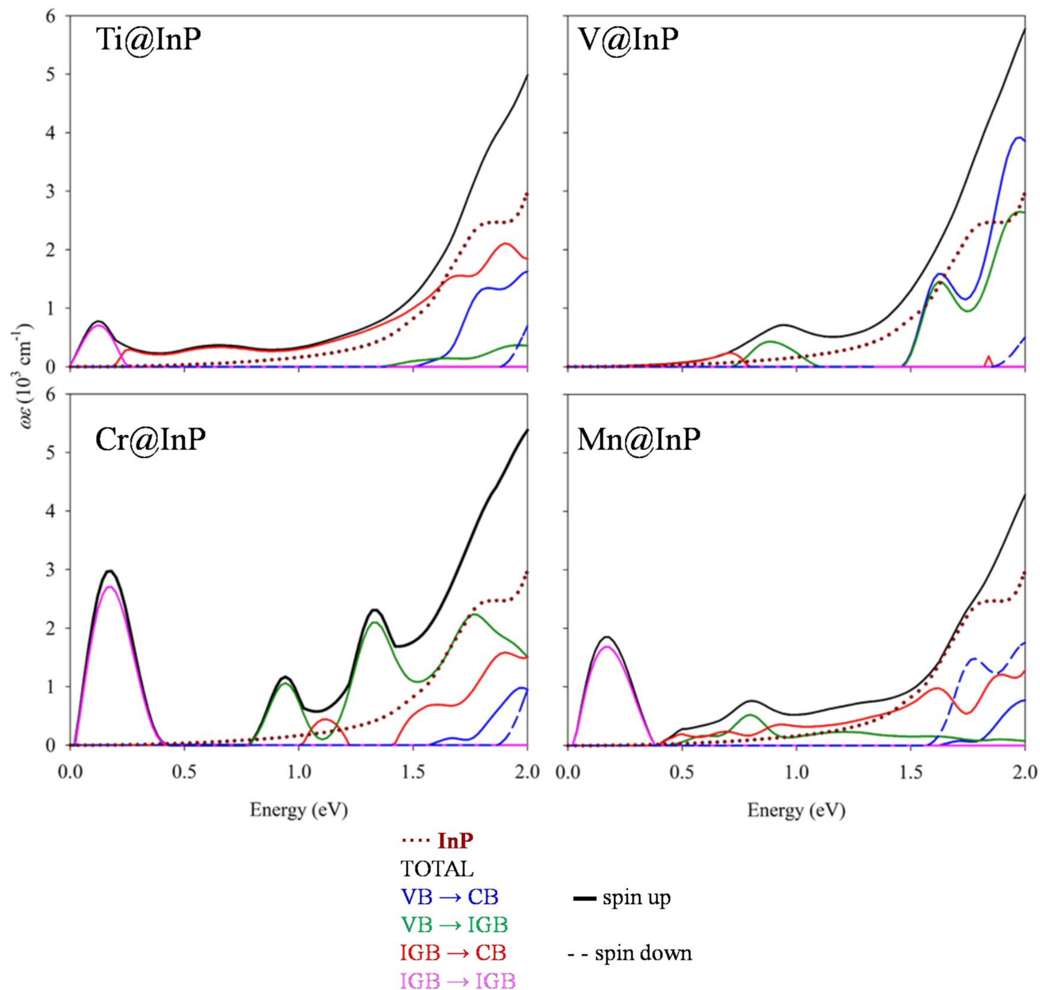

Figure 8. Partial contributions to the imaginary part of the dielectric function ε, multiplied by the frequency ω, for TM@InP.

4. Conclusions

The structural, electronic and sunlight-absorption properties of transition metal-hyperdoped InP materials, i.e., TM@InP (TM = Ti, V, Cr, Mn), with the general formula $TM_xIn_{1-x}P$ (x = 0.03) wereinvestigated using ab initio methods. The equilibrium structure of these compounds was not importantly distorted due to the TM's presence, while the energetic of the hyperdoping process was compatible with the possibility to experimentally obtain TM@InP materials under adequate conditions. The bandgap underestimation problem of the common density-functional theory methods (DFT) was bypassed by using more accurate electronic structure methods, such as many-body perturbation methods in the G_0W_0 approach and DFT along with the Dudarev approach (PBE+U, U_{eff} = 15 eV) to deeply assess the electronic structure of InP and TM@InP compounds. Both methods provided similar electronic structure information. The G_0W_0 approach needs high computational requirements; thus, the electronic structure and optical absorption features were calculated by using DFT+U, while G_0W_0

was used as benchmark method. For the spin-up component, the electronic structure results can be interpreted in concordance with crystal field theory, i.e., TM 3*d* states split by the near tetrahedral environments in two manifolds: a low-energy e_g doublet and a high-energy t_{2g} triplet. Briefly, TM hyperdoping leads to a bandgap decrease for TM = Ti, V, although those levels are mainly located in the forbidden gap of the host InP material. For TM = Cr, Mn (for TM = Mn, such conclusions are only obtained with PBE+*U*), the high-energy t_{2g} triplets meet the requirements to be defined as an IGB. Thus, a theoretical efficiency ~ 60% could be obtained based on its electronic structure, which leads to a considerable improvement with respect to the theoretical maximum conversion efficiency ~ 33% based on the SQ model. Finally, the light absorption features were investigated through the imaginary part of the dielectric function. The optical absorption coefficients are greatly enhanced in the whole range of energy for photovoltaic applications and the absorption range is also largely extended up to 0.5 eV due to new electronic transitions, where TM 3*d* states take part at donor or acceptor levels. The best results are obtained for Cr@InP, for which the gained photo-absorption considerably benefits from the two photons process induced by the IGB.

Supplementary Materials: The following are available online at http://www.mdpi.com/2079-4991/10/2/283/s1, Figure S1: Calculated bandgap at Γ-point for InP by using PBE+*U* formalism (U_{eff} = 5, 8, 10, 15, 18 eV). The crystal structure optimizations were performed using the PBEsol. The blue and green dotted lines stand for G_0W_0 and experimental value; Figure S2: Electronic band structure (left) and the density of states (right) of InP were calculated with the G_0W_0 approach, along with the main energy differences at Γ-point. The zero energy was set to the Fermi level (the black dotted line). The spin-up and spin-down bands and DOS are not given separately, as both contributions are the same for the native InP material; Figure S3: Electronic band structure of TM@InP (TM = Ti, V, Cr, Mn) calculated with the G_0W_0 approach, along with the main energy differences at Γ-point. The zero energy was set at the Fermi level (black dotted line); Figure S4: Density of states of TM@InP (TM = Ti, V, Cr, Mn) calculated with the G_0W_0 approach. The zero energy was set at the Fermi level (the black dotted line); Table S1: Crystal Structure of TM (TM = Ti, V, Cr, Mn), In and P atoms.

Author Contributions: P.W. and P.P. designed the project. P.S.-P. and G.G. performed theoretical calculations. G.G. wrote the paper. All authors contributed to the concept and revised manuscript. All authors have read and agree to the published version of the manuscript.

Funding: This research was partially funded by Ministerio de Economía y Competitividad through the project SEHTOP-QC (ENE2016-77798-C4-4-R) and by Universidad Politécnica de Madrid through the project DNSMEP (VJIDOCUPM19GGM).

Acknowledgments: The author thankfully acknowledges the computer resources, technical expertise and assistance provided by the Supercomputing and Visualization Center of Madrid (CeSViMa). The statements made herein are solely the responsibility of the authors.

Conflicts of Interest: The authors declare no conflict of interest.

References

1. Rasukkannu, M.; Velauthapillai, D.; Bianchini, F.; Vajeeston, P. Properties of Novel Non-Silicon Materials for Photovoltaic Applications: A First-Principle Insight. *Materials* **2018**, *11*, 2006. [CrossRef]
2. Unold, T.; Schock, H.W. Nonconventional (Non-Silicon-Based) Photovoltaic Materials. *Annu. Rev. Mater. Res.* **2011**, *41*, 297–321. [CrossRef]
3. Henry, C.H. Limiting efficiencies of ideal single and multiple energy gap terrestrial solar cells. *J. Appl. Phys.* **1980**, *51*, 4494–4500. [CrossRef]
4. Yuan, L.D.; Deng, H.X.; Li, S.S.; Wei, S.H.; Luo, J.W. Unified theory of direct or indirect band-gap nature of conventional semiconductors. *Phys. Rev. B* **2018**, *98*, 245203. [CrossRef]
5. Tanabe, K. A Review of Ultrahigh Efficiency III-V Semiconductor Compound Solar Cells: Multijunction Tandem, Lower Dimensional, Photonic Up/Down Conversion and Plasmonic Nanometallic Structures. *Energies* **2009**, *2*, 504–530. [CrossRef]
6. Friedman, D.J. Progress and challenges for next-generation high-efficiency multijunction solar cells. *Curr. Opin. Solid State Mater. Sci.* **2010**, *14*, 131–138. [CrossRef]
7. Mokkapati, S.; Jagadish, C. III-V compound SC for optoelectronic devices. *Mater. Today* **2009**, *12*, 22–32. [CrossRef]

8. Teran, A.S.; Lim, W.; Lee, I.; Philips, J.D. Energy Harvesting for GaAs Photovoltaics Under Low-Flux Indoor Lighting Conditions. *IEEE Trans. Electron Devices* **2016**, *63*, 2820–2825. [CrossRef]
9. Keavney, C.J.; Haven, V.E.; Vernon, S.M. Emitters structures in MOCVD InP solar cells. *IEEE Conf. Photovolt. Spec.* **1990**, 141–144.
10. Yin, X.; Battaglia, C.; Lin, Y.; Chen, K.; Hettick, M.; Zheng, M.; Chen, C.Y.; Kiriya, D.; Javey, A. 19.2% Efficient InP Heterojunction Solar Cell with Electron-Selective TiO2 Contact. *ACS Photonics* **2014**, *1*, 1245–1250. [CrossRef]
11. Coutts, T.J.; Naseem, S. High efficiency indium tin oxide/indium phosphide solar cells. *Appl. Phys. Lett.* **1985**, *46*, 164–166. [CrossRef]
12. Wagner, S.; Shay, J.L.; Bachmann, K.J.; Buehler, E. p−InP/n−CdS solar cells and photovoltaic detectors. *Appl. Phys. Lett.* **1975**, *26*, 229–230. [CrossRef]
13. Sai Gautam, G.; Senftle, T.P.; Alidoust, N.; Carter, E.A. Novel Solar Cell Materials: Insights from First-Principles. *J. Phys. Chem. C* **2018**, *122*, 27107–27126. [CrossRef]
14. Luque, A.; Martí, A. Increasing the Efficiency of Ideal Solar Cells by Photon Induced Transitions at Intermediate Levels. *Phys. Rev. Lett.* **1997**, *78*, 5014–5017. [CrossRef]
15. Luque, A.; Marti, A. Photovoltaics: Towards the intermediate band. *Nat. Photon.* **2011**, *5*, 137–138. [CrossRef]
16. Luque, A.; Marti, A.; Stanley, C. Understanding intermediate-band solar cells. *Nat. Photon.* **2012**, *6*, 146–152. [CrossRef]
17. Palacios, P.; Fernández, J.J.; Sánchez, K.; Conesa, J.C.; Wahnón, P. First-principles investigation of isolated band formation in half-metallic TixGa1-xP (x = 0.3125–0.25). *Phys. Rev. B* **2006**, *73*, 085206. [CrossRef]
18. Tablero, C.; Palacios, P.; Fernández, J.J.; Wahnón, P. Properties of intermediate band materials. *Sol. Energy Mater. Sol. Cells* **2005**, *87*, 323–331. [CrossRef]
19. Palacios, P.; Sánchez, K.; Conesa, J.C.; Wahnón, P. First principles calculation of isolated intermediate bands formation in a transition metal-doped chalcopyrite-type semiconductor. *Phys. Stat. Sol.* **2006**, *203*, 1395–1401. [CrossRef]
20. Palacios, P.; Sánchez, K.; Conesa, J.C.; Fernández, J.J.; Wahnón, P. Theoretical modelling of intermediate band solar cell materials based on metal-doped chalcopyrite compounds. *Thin Solid Film* **2007**, *515*, 6280–6284. [CrossRef]
21. Aguilera, I.; Palacios, P.; Wahnón, P. Optical properties of chalcopyrite-type intermediate transition metal band materials from first principles. *Thin Solid Film* **2008**, *516*, 7055–7059. [CrossRef]
22. Lucena, R.; Aguilera, I.; Palacios, P.; Wahnón, P.; Conesa, J.C. Synthesis and Spectral Properties of Nanocrystalline V-Substituted In2S3, a Novel Material for More Efficient Use of Solar Radiation. *Chem. Mater.* **2008**, *20*, 5125–5127. [CrossRef]
23. Wahnón, P.; Conesa, J.C.; Palacios, P.; Lucena, R.; Aguilera, I.; Seminovski, Y.; Fresno, F. V-doped SnS2: A new intermediate band material for a better use of the solar spectrum. *Phys. Chem. Chem. Phys.* **2011**, *13*, 20401–20407. [CrossRef] [PubMed]
24. Lucena, R.; Conesa, J.C.; Aguilera, I.; Palacios, P.; Wahnón, P. V-substituted In2S3: An intermediate band material with photocatalytic activity in the whole visible light range. *J. Mater. Chem. A* **2014**, *2*, 8236–8245. [CrossRef]
25. Seminóvski, Y.; Palacios, P.; Conesa, J.C.; Wahnón, P. Thermodynamics of zinc insertion in CuGaS2:Ti, used as a modulator agent in an intermediate-band photovoltaic material. *Comput. Theor. Chem.* **2011**, *975*, 134–137. [CrossRef]
26. Seminóvski, Y.; Palacios, P.; Wahnón, P. Intermediate band position modulated by Zn addition in Ti doped CuGaS2. *Thin Solid Film* **2011**, *519*, 7517–7521. [CrossRef]
27. Seminovski, Y.; Palacios, P.; Wahnón, P. Obtaining an intermediate band photovoltaic material through the Bi insertion in CdTe. *Sol. Energy Mater. Sol. Cells* **2013**, *114*, 99–103. [CrossRef]
28. Seminovski, Y.; Palacios, P.; Wahnón, P. Analysis of SnS2 hyperdoped with V proposed as efficient absorber material. *J. Phys. Condens. Matter* **2014**, *26*, 395501. [CrossRef]
29. Castellanos-Águila, J.E.; Palacios, P.; Conesa, J.C.; Arriaga, J.; Wahnón, P. Theoretical band alignment in an intermediate band chalcopyrite based material. *Appl. Surf. Sci.* **2017**, *424*, 132–136. [CrossRef]
30. Palacios, P.; Aguilera, I.; Wahnón, P.; Conesa, J.C. Thermodynamics of the Formation of Ti- and Cr-doped CuGaS2 Intermediate-band Photovoltaic Materials. *J. Phys. Chem. C* **2008**, *112*, 9525–9529. [CrossRef]

31. Sánchez, K.; Aguilera, I.; Palacios, P.; Wahnón, P. Assessment through first-principles calculations of an intermediate-band photovoltaic material based on Ti-implanted silicon: Interstitial versus substitutional origin. *Phys. Rev. B* **2009**, *79*, 165203. [CrossRef]
32. Sánchez, K.; Aguilera, I.; Palacios, P.; Wahnón, P. Formation of a reliable intermediate band in Si heavily coimplanted with chalcogens (S, Se, Te) and group III elements (B, Al). *Phys. Rev. B* **2010**, *82*, 165201. [CrossRef]
33. Aguilera, I.; Palacios, P.; Wahnón, P. Understanding Ti intermediate-band formation in partially inverse thiospinel MgIn2S4 through many-body approaches. *Phys. Rev. B* **2011**, *84*, 115106. [CrossRef]
34. García, G.; Casanova-Páez, M.; Palacios, P.; Menéndez-Proupin, E.; Wahnón, P. First principle study of V-implantation in highly-doped silicon materials. *Comput. Mater. Sci.* **2017**, *136*, 207–215. [CrossRef]
35. Garcia-Hemme, E.; García, G.; Palacios, P.; Montero, D.; García-Hernansanz, R.; González-Díaz, G.; Wahnón, P. Vanadium supersaturated silicon system: A theoretical and experimental approach. *J. Phys. D Appl. Phys.* **2017**, *50*, 495101. [CrossRef]
36. García, G.; Palacios, P.; Menéndez-Proupin, E.; Montero-Alejo, A.L.; Conesa Wahnón, P. Influence of chromium hyperdoping on the electronic structure of CH3NH3PbI3 perovskite: A first-principles insight. *Sci. Rep.* **2018**, *8*, 2511.
37. Olea, J.; del Prado, A.; García-Hemme, E.; García-Hernansanz, R.; Montero, D.; González-Díaz, G.; Gonzalo, J.; Siegel, J.; López, E. Strong subbandgap photoconductivity in GaP implanted with Ti. *Prog. Photovolt. Res. Appl.* **2018**, *26*, 214–222. [CrossRef]
38. Palacios, P.; Wahnón, P.; Tablero, C. Ab initio phonon dispersion calculations for TixGanAsm and TixGanPm compounds. *Comput. Mater. Sci.* **2005**, *33*, 118–124. [CrossRef]
39. Palacios, P.; Wahnón, P.M.; Pizzinato, S.; Conesa, J.C. Energetics of formation of TiGa3As4 and TiGa3P4 intermediate band materials. *J. Chem. Phys.* **2006**, *124*, 014711. [CrossRef] [PubMed]
40. Hu, J.M.; Wang, D.; Zhao, W.M.; Gu, Y.; Bu, K.; Pan, J.; Quin, P.; Zhang, X.; Huang, F. Intermediate Band Material of Titanium-Doped Tin Disulfide for Wide Spectrum Solar Absorption. *Inorg. Chem.* **2018**, *57*, 3956–3962. [CrossRef]
41. Palacios, P.; Aguilera, I.; Sánchez, K.; Conesa, J.C.; Wahnón, P. Transition-Metal-Substituted Indium Thiospinels as Novel Intermediate-Band Materials: Prediction and Understanding of Their Electronic Properties. *Phys. Rev. Lett* **2008**, *101*, 046403. [CrossRef] [PubMed]
42. Palacios, P.; Sánchez, K.; Wahnón, P.; Conesa, J.C. Characterization by Ab Initio Calculations of an Intermediate Band Material Based on Chalcopyrite Semiconductors Substituted by Several Transition Metals. *J. Sol. Energy Eng.* **2006**, *129*, 314–318. [CrossRef]
43. Aguilera, I.; Palacios, P.; Wahnón, P. Enhancement of optical absorption in Ga-chalcopyrite-based intermediate-band materials for high efficiency solar cells. *Sol. Energy Mater. Sol. Cells* **2010**, *94*, 1903–1906. [CrossRef]
44. Ullah, S.; Ullah, H.; Bouhjar, F.; Mollar, M.; Marí, B. Synthesis of in-gap band CuGaS2:Cr absorbers and numerical assessment of their performance in solar cells. *Sol. Energy Mater. Sol. Cells* **2018**, *180*, 322–327. [CrossRef]
45. Chan, M.K.Y.; Ceder, G. Efficient Band Gap Prediction for Solids. *Phys. Rev. Lett.* **2010**, *105*, 196403. [CrossRef] [PubMed]
46. Dudarev, S.L.; Botton, G.A.; Savrasov, S.Y.; Humphreys, C.J.; Sutton, A.P. Electron-energy-loss spectra and the structural stability of nickel oxide: An LSDA+U study. *Phys. Rev. B* **1998**, *57*, 1505–1509. [CrossRef]
47. Oba, F.; Kumagai, Y. Design and exploration of semiconductors from first principles: A review of recent advances. *Appl. Phys. Express* **2018**, *11*, 060101. [CrossRef]
48. Hedin, L. New Method for Calculating the One-Particle Green's Function with Application to the Electron-Gas Problem. *Phys. Rev.* **1965**, *139*, A796–A823. [CrossRef]
49. Kresse, G.; Hafner, J. Ab initio} molecular dynamics for liquid metals. *Phys. Rev. B* **1993**, *47*, 558–561. [CrossRef]
50. Kresse, G.; Furthmüller, J. Efficient iterative schemes for ab initio total-energy calculations using a plane-wave basis set. *Phys. Rev. B* **1996**, *54*, 11169–11186. [CrossRef]
51. Perdew, J.P.; Ruzsinszky, A.; Csonka, G.I.; Vydrov, O.A.; Scuseria, G.E.; Constantin, L.A.; Zhou, X.; Burke, K. Restoring the Density-Gradient Expansion for Exchange in Solids and Surfaces. *Phys. Rev. Lett.* **2008**, *100*, 136406. [CrossRef] [PubMed]

52. Luque, A.; Martí, A.; Antolín, E.; Tablero, C. Intermediate bands versus levels in non-radiative recombination. *Phys. B Condens. Matter.* **2006**, *382*, 320–327. [CrossRef]
53. Bahuguna, B.P.; Sharma, R.O.; Saini, L.K. The LDA+U calculation of electronic band structure of GaAs. *AIP Conf. Proc.* **2016**, *1728*, 020601.
54. Iandelli, A. Sulla struttura dei composti InP, InAs e InSb. *Gazz. Chim. Ital.* **1941**, *71*, 58–62.
55. Zhang, S.B.; Northrup, J.E. Chemical potential dependence of defect formation energies in GaAs: Application to Ga self-diffusion. *Phys. Rev. Lett.* **1991**, *67*, 2339–2342. [CrossRef]
56. Karki, V.; Bhattachary, D.; Rao, T.V.C.; Alamelu, D. Depth distribution of Mn in Mn doped GaAs using secondary ion mass spectrometry. *Vac. Sci. Technol. B* **2016**, *34*, 03H125. [CrossRef]
57. Cotton, F.A. I-Ligand field theory. *J. Chem. Educ.* **1964**, *41*, 466. [CrossRef]
58. Deng, F.; Cao, H.; Liang, L.; Li, J.; Gao, J.; Zhang, H.; Qin, R.; Liu, C. Determination of the basic optical parameters of ZnSnN2. *Opt. Lett.* **2015**, *40*, 1282–1285. [CrossRef]

© 2020 by the authors. Licensee MDPI, Basel, Switzerland. This article is an open access article distributed under the terms and conditions of the Creative Commons Attribution (CC BY) license (http://creativecommons.org/licenses/by/4.0/).

3.2. Second publication

Acta Materialia 197 (2020) 316–329

Contents lists available at ScienceDirect

Acta Materialia

journal homepage: www.elsevier.com/locate/actamat

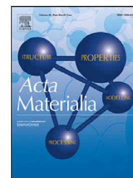

Spinel-Type nitride compounds with improved features as solar cell absorbers

Pablo Sánchez-Palencia [a,b], Gregorio García [a,b,*], José C. Conesa [c], Perla Wahnón [a,b], Pablo Palacios [a,d]

[a] Instituto de Energía Solar, ETSI Telecomunicación, Universidad Politécnica de Madrid, Ciudad Universitaria, s/n, 28040 Madrid, Spain
[b] Departamento de Tecnología Fotónica y Bioingeniería, ETSI Telecomunicación, Universidad Politécnica de Madrid, Ciudad Universitaria, s/n, 28040 Madrid, Spain
[c] Instituto de Catálisis y Petroleoquímica, Consejo Superior de Investigaciones Científicas, Marie Curie 2, 28049 Madrid, Spain
[d] Departamento de Física aplicada a las Ingenierías Aeronáutica y Naval, ETSI Aeronáutica y del Espacio, Universidad Politécnica de Madrid, Pz. Cardenal Cisneros, 3, 28040 Madrid, Spain

A R T I C L E I N F O

Article history:
Received 23 March 2020
Revised 7 July 2020
Accepted 12 July 2020
Available online 19 July 2020

Keywords:
IV-spinel nitrides
Electronic structure
In-gap-band
Photovoltaics
Ab-initio

A B S T R A C T

Ternary spinel nitrides are a new class of semiconductor materials with tunable bandgap in the visible range. In this work, we report a rational design of spinel-type nitride compounds with improved features as solar cell absorber materials by way of the in-gap-band (IGB) concept. For this purpose, a systematic screening on the effect of transition metal (M = Sc, Ti, V, Cr, Mn, Fe, Co, Ni, Cu, Zn, Nb, Mo) hyper-doping on the crystal and electronic structure properties of germanium (Ge) and tin (Sn) spinel nitrides (γ-$(M_mSn_{x-m}Ge_{1-x})_3N_4$, x = 0.5, m = 0.042, 0.083) was carried out through accurate *ab-initio* methods. The analysis of the electronic structure reveals that M-hyperdoped ternary spinel nitrides with M = Cr, Co, Cu show an IGB with the adequate properties to allow two extra photon absorption processes. A detailed study of the sunlight absorption properties, and maximum photovoltaic efficiencies reveal that Co-hyperdoped spinel is an excellent candidate to be used in photovoltaic devices as absorber material, with maximum photovoltaic efficiency of ~ 55%. Overall, our results suggest that it would be possible to design new ternary spinel-type nitride materials with improved absorption properties suitable for potential use in photovoltaic applications.

© 2020 Acta Materialia Inc. Published by Elsevier Ltd. All rights reserved.

1. Introduction

IV-nitride compounds, mainly silicon nitride Si_3N_4, are well-known ceramics that are widely used in the industry. Si_3N_4 owns many desirable properties such as high thermal stability, extreme resistance to surface oxidation, and mechanical and optical properties, which are adequate for industrial applications like turbine engines, diesel engines and industrial heat exchangers [1]. Group 14 nitrides exist in two energetically favorable phases alpha (α-) and (β-) beta, which have hexagonal crystal structures with different stacking patterns of the layered atoms perpendicular to the c axis [2,3]. The discovery of dense nitrides with spinel structure (such as γ-Si_3N_4 and γ-Ge_3N_4) at high temperature and pressure [4,5] has stimulated a new research area devoted to the study of IV-nitride semiconductors with cubic spinel structure as potential candidates for optoelectronic devices, *e.g.* field effect transistors, light emitting diodes or lasers [6–10]. So far, the binary nitride compounds with spinel structure γ-A_3N_4 (A= Si, Ge, Sn) have been synthesized with experimentally measured properties [5,11,12]. Unlike γ-Si_3N_4 and γ-Ge_3N_4, γ-Sn_3N_4 can be easily synthesized at ambient pressure [13,14]. In the cubic spinel structure, group 14 cations (Si, Ge or Sn) adopt both tetrahedral and octahedral coordination (see Fig. 1), thereby presenting a unique structure. In comparison with hexagonal phases, spinel structures offer increased hardness (highly adequate for mechanical applications) as well as a smaller direct bandgap (E_g) in the UV range, that allows these materials to be used for optoelectronic applications [3,6,7]. Several studies have been carried out to deeply assess the electronic structure and optical properties of γ-Si_3N_4, γ-Ge_3N_4 and γ-Sn_3N_4 [9,10,12,14–20], as well as their solid solutions (ternary nitrides) [18,21–23]. These results suggest that solid solutions of IV-nitrides with spinel structure (with general formula $(A_xA'_{1-x})_3N_4$, being A, A' = Si, Ge, Sn) are excellent candidates for a new class of materials with tunable bandgap and hardness by controlling their chemical composi-

* Corresponding author at: Instituto de Energía Solar, ETSI Telecomunicación, Universidad Politécnica de Madrid, Ciudad Universitaria, s/n, 28040 Madrid, Spain.
E-mail address: ggmoreno@etsit.upm.es (G. García).

https://doi.org/10.1016/j.actamat.2020.07.034
1359-6454/© 2020 Acta Materialia Inc. Published by Elsevier Ltd. All rights reserved.

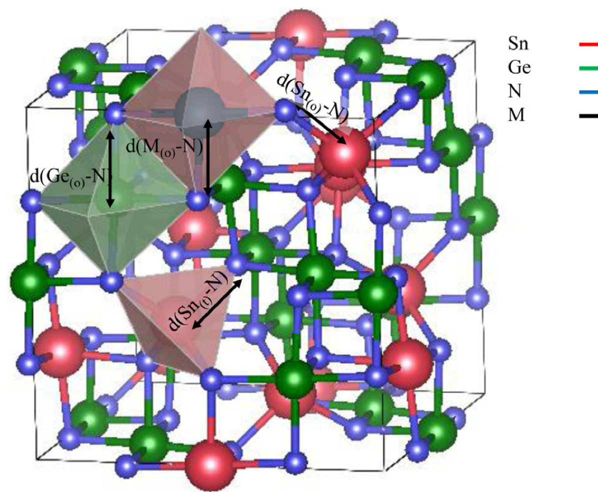

Fig. 1. Crystal structure of γ-$(M_mSn_{0.5}Ge_{0.5})_3N_4$ (m = 0.042). For γ-Ge_3N_4 / γ-Sn_3N_4 / γ-$(Sn_xGe_{1-x})_3N_4$ Sn and M / Ge and M / M atoms would be replaced by Ge / Sn / Sn atoms. Tetrahedral and octahedral environments for $A_{(t)}$ and $A_{(o)}$ atoms, respectively, are also displayed.

tion. Moreover, it has been also shown that the electronic structure of γ-Si_3N_4, γ-Ge_3N_4 can be tailored by chemical doping [24–29]. In addition to tunable bandgap in the visible range and improved hardness, spinel-type IV-nitrides also display photocurrent generation [30], which makes them suitable to be used as the active absorber material in solar cell devices. Recently, Wang et al. have pointed to semiconductors with a spinel structure as potential candidates to expand the scope of materials with photovoltaic applications beyond conventional semiconductors and perovskites [31].

Hence, this work is focused in the design of spinel-type IV-nitride compounds as highly efficient solar absorber materials. Based on the bandgap values of binary compounds [9,12,14–19,32], only γ-Sn_3N_4 (E_g = 1.15–1.55 eV based on *ab-initio* and experimental data) would be suitable as sunlight absorber material, since the bandgaps of γ-Si_3N_4 (E_g ~ 5.10 eV) and γ-Ge_3N_4 (E_g ~ 3.50 eV) are too high to be used in photovoltaic devices [33]. For γ-Sn_3N_4, according to the Shockley-Queisser (SQ) model, the theoretical maximum solar conversion efficiency would be ~32.5–31.0% for an energy bandgap of 1.15–1.55 eV [33]. To our knowledge, proposals for the use of IV-nitride semiconductors with spinel structure for solar energy conversion are rather scarce. Caskey et al. studied the semiconducting properties of γ-Sn_3N_4 by thin-film experiments and first-principle calculations [12], while Zakutayev reviewed the recent advances in the design of semiconducting nitrides [34]. Regarding to IV-nitrides with spinel structure, this review only mentions the results previously published by Caskey et al. [12]. These results suggest that γ-Sn_3N_4 have a large hole effective mass, which would be responsible for the short hole diffusion length. This problem could be fixed by alloying with other group-IV metal nitrides, *i.e.* by using ternary nitrides in the spinel structure, which would increase the bandgap up to 2.0–3.5 eV [12,18]. Therefore, further investigation in the search of new IV-nitrides with spinel structure as highly efficient solar absorber materials is needed.

Among others, the photovoltaic efficiency can be improved through sub-bandgap absorptions by way of the in-gap-band (IGB) concept, which consists in a partially filled narrow (but delocalized enough) band located between the valence and the conduction bands (VB and CB, respectively) of the host semiconductor. In fact, the upper limit efficiency of an IGB solar cell could reach theoretical efficiencies up to 63.1% [35–37]. The first step in the search of new IGB-materials is the selection of an adequate host semiconductor with bandgap ~ 2.0 eV, which would lead to the highest theoretical efficiencies [35]. Based on the results of Boyko et al. [18], together with the need of alloying γ-Sn_3N_4, γ-$(Sn_xGe_{1-x})_3N_4$ with x = 0.5 (theoretical estimated bandgap $E_g \simeq$ 2.2 eV) has been proposed as host semiconductor material. From that point on, IGB materials can be obtained through the substitutional hyperdoping of some cations by a transition metal (M) [38–64]. In this way, *d*-orbitals of M atoms might be located within the bandgap of semiconductors allowing the formation of an isolated energy band, while the filling of the IGB can be finetuned through the adequate selection of M dopant. High concentrations of IGB states (*i.e.*, high transition metal doping concentrations) are required to produce high absorption coefficients for those sub-bandgap absorptions and to avoid non radiative recombination obtained through the formation of a highly delocalized energy band. This concentration is beyond Mott limit and much higher than the solubility limit. [35–37,65] For that reason, we report a detailed *ab-initio* study of structural and electronic structure related properties of the spinel type IV-nitride semiconductors and their M-hyperdoped compounds according to the general formula γ-$(M_mSn_{x-m}Ge_{1-x})_3N_4$, being x = 0.5 and m = 0.042, 0.083. In the search of the adequate transition metal, we have systematic studied 3*d*-block elements (Sc, Ti, V, Cr, Mn, Fe, Co, Ni, Cu, Zn) along with the most abundant 4*d*-block ones (Nb, Mo) as dopant elements.

2. Theoretical details

The calculations here proposed have been performed within the PAW method [66,67] by using the Vienna *ab initio* simulation package (VASP) [68,69]. Firstly, structure optimizations were performed using the PBE functional [70]. Forces and total energies are converged to 0.01 eV Å^{-1}, 10^{-4} eV, respectively. The Brillouin zone has been sampled using a 8 × 8 × 8 Γ-centered grid (12 × 12 × 12 for electronic structure calculations). Regarding to electronic structure calculations, the bandgap is one of the more important parameters when characterizing a semiconductor as solar cell absorber material. Hence, a proper description of the electronic structure is necessary to obtain accurate results. Several works have reported the electronic structure of spinel type IV-nitrides (γ-A_3N_4, A = Si, Ge, Sn) using density functional methods (DFT) methods [3,9,10,14,22,24,25]. It is well known that common DFT methods considerably underestimate the bandgap [71]. In fact, previously predicted bandgap values are considerably lower than experimental ones. Boyko et al. reported that electronic bandgap values with significantly improved accuracy can be obtained when the m-BJ exchange functional is used [18]. Several works [12,19] have investigated the electronic structure of IV-nitrides in the spinel phase using *GW* calculations, that were carried out to correct PBE eigenvalues without further interactions, *i.e.*, with the G_0W_0 approach [72]. As result, calculated G_0W_0 bandgaps agree with experiments. In addition, it has been successfully proven that this method yields results in good agreement with experimental results for IGB materials [55,56]. However, in this work a single shot G_0W_0 was not able to correctly estimate bandgap values compared with the experimental ones Section 3.1. Thus, self-consistent GW_0 (sc-GW_0) calculations were carried out to correct PBE eigenvalues, where the quasi-particle energies in the Green functions are iterated. GW_0 approach was carried out with a Γ-centered 4 × 4 × 4 k-point mesh to sample the Brillouin zone, 1024 bands and an energy cutoff of 100 eV. Due to the high computational cost of self-consistent GW_0 approach, a limitation of 10 iterations for the Green function was set. Even though, self-consistent GW_0 eigenvalues usually converge in about 4/5 iterations [73]. Finally, starting from PBE wave functions and quasiparticle energies (sc-GW_0), optical properties have

been assessed by solving the Bethe-Salpeter equation (BSE) as implemented in VASP code [74,75].

The crystal structure of γ-A_3N_4 (A = Ge or Sn) was defined through a unit cell containing 56 atoms ($A_{24}N_{32}$), belonging to the 227 (*Fd*-3m) space group, wherein 16 A cations (66%) adopt an octahedral ($A_{(o)}$) coordination, while 8 A cations (33%) are in a tetrahedral environment ($A_{(t)}$), see Fig. 1. Two parameters are the key when optimizing the unit cell: the lattice constant and the anion bonding parameter. Both should be optimized to achieve minima equilibrium energies and inter-atomic forces [18]. Our target model for γ-$(Sn_{0.5}Ge_{0.5})_3N_4$ is built taking into account that the larger cation (Sn) fills the tetrahedral positions before the octahedral ones [18]. Therefore, there are 12 $Ge_{(o)}$, 4 $Sn_{(o)}$ and 8 $Sn_{(t)}$, meaning that several geometrical configurations can be obtained depending on the different relative position of those 4 Sn atoms among the octahedral sites. These geometrical configurations were defined using the combinatorial methodology implemented in SOD (Site Occupancy Disorder) program [76]. The SOD methodology would also allow to obtain the configurational entropy. In our case, one non-degenerate configuration has a much lower energy than the rest. Therefore, both the energy and the free energy of the systems should be identical to the energy of that configuration, *i.e.*, the configurational entropy would be zero. Hence, we have only focused on those structures with the lowest energy, which also own the highest space group symmetry (213). Note that this ordering of group-14 atoms in γ-$(Sn_{0.5}Ge_{0.5})_3N_4$ is inverted with respect to previously studied γ-$(SiGe)_3N_4$ ternary spinels, where tetrahedral positions are occupied by Ge [22,23]. In this way, in correlation with the atomic radii (R_i) trend ($R_{Sn} > R_{Ge} > R_{Si}$) [77]. Additionally, the crystal structure of the "*reversed* γ-$(Sn_{0.5}Ge_{0.5})_3N_4$ spinel" has been also optimized. For this *reversed* structure, tetrahedral positions are occupied by Ge atoms, *i.e.*, there are 12 $Sn_{(o)}$, 4 $Ge_{(o)}$ and 8 $Ge_{(t)}$. The energy difference between *reversed* γ-$(Sn_{0.5}Ge_{0.5})_3N_4$ and γ-$(Sn_{0.5}Ge_{0.5})_3N_4$ spinels is ΔE = [E(*reversed* γ-$(Sn_{0.5}Ge_{0.5})_3N_4$ *spinel*] – E[γ-$(Sn_{0.5}Ge_{0.5})_3N_4$] = 5.17 eV/unit cell. This ΔE points out that the stability of the *reversed* γ-$(Sn_{0.5}Ge_{0.5})_3N_4$ spinel is considerably smaller. The crystal structures of M-hyperdoped compounds γ-$(M_mSn_{0.5-m}Ge_{0.5})_3N_4$ were built from γ-$(Sn_{0.5}Ge_{0.5})_3N_4$, with Sn and Ge keeping their positions as defined above by replacing one (or two) $Sn_{(o)}$ atom(s) by M, which led to M concentration of m = 0.042 (m = 0.083), *i.e.* a concentration of ~ $1.5 \cdot 10^{21}$ cm^{-3} (~ $2.9 \cdot 10^{21}$ cm^{-3}). Transition metal concentrations here studied are higher than the one required to produce high absorption coefficients for new subbandgap absorptions and to avoid non radiative recombination (> $5 \cdot 10^{19}$ cm^{-3}, known as Mott Limit) [35–37,65]. For m = 0.083 different crystal structures were defined using the SOD package, focusing our interest on those structures with the lowest energy and the highest symmetry.

3. Results

3.1. Crystal structure and stability properties of γ-$(Sn_{0.5}Ge_{0.5})_3N_4$ and γ-$(M_mSn_{0.5-m}Ge_{0.5})_3N_4$

Group 14 nitrides with spinel structure have been extensively studied through theoretical and experimental methods. In fact, both γ-Ge_3N_4 and γ-Sn_3N_4 have been synthesized. Both compounds represent the upper and lower limits of the properties here characterized for γ-$(Sn_{0.5}Ge_{0.5})_3N_4$ and γ-$(M_mSn_{0.5-m}Ge_{0.5})_3N_4$. Therefore, the results obtained for γ-Ge_3N_4 and γ-Sn_3N_4 have been also included for comparative purposes. Fig. 2 summarizes the lattice cells parameters (a) and the most representative bond lengths (d) for the optimized crystal structures. As seen there, calculated values for γ-Ge_3N_4 and γ-Sn_3N_4 are in good agreement with the experimental data [11,78], and the deviations are less than 2%. For γ-$(Sn_{0.5}Ge_{0.5})_3N_4$, the lattice parameter (a = 8.738 Å) is increased respect to γ-Ge_3N_4 due to the larger atomic radius of Sn than Ge.

The substitutional doping of $Sn_{(o)}$ by a M atom does not lead to important changes in the lattice cell parameter. For hyperdoped spinels with M = Sc, Ti, Cu, Zn, Nb and Mo, d($M_{(o)}$-N) are larger than d($Sn_{(o)}$-N) in the host material, while d($M_{(o)}$-N) are shorter for the remaining M atoms. Nonetheless, all hyperdoped compounds follow the same trend: most structural parameters slightly decrease upon Sn replacement by a M atom. Lattice parameter changes with respect to the host material γ-$(Sn_{0.5}Ge_{0.5})_3N_4$ are lower than 0.07 Å / 0.11 Å for m = 0.042/0.083, while d($Ge_{(o)}$-N) and d($Sn_{(o)}$-N) are shortened by ~ 0.02/0.03 Å and 0.01/0.02 Å, respectively. The decrease in the octahedral voids around M promotes that d($Sn_{(t)}$-N) are lengthened ~ 0.08 Å for both M concentrations. Although Fig. 2 displays average bond-length values, six d($M_{(o)}$-N) distances are not equivalent for M=V, Cr, Fe, Co, Nb and Mo. In these systems, there is a compression of the octahedral environment around M along the longitudinal z-axis. Therefore, two d($M_{(o)}$-N) bond lengths (those located along this longitudinal axis) are slightly shortened respect to the remaining ones located in the xy plane. These small distortions will influence the electronic structure of M-hyperdoped spinels.

It is well known that nitrides are difficult to synthesize in the laboratory. Main problems related with the synthesis of nitrides is related with the low chemical reactivity of the N_2 molecule. For this reason, nitrides generally decompose at high temperature; and they must be synthesized in oxygen- and water-free atmospheres. For these reasons there are several works dealing with computational materials discovery of new nitrides materials by using high-throughput computational methods. However, these methods are out the scope of this manuscript [79,80]. Therefore, in this paper, the relative stability of compounds here studied has been assessed from both energetic and bonding strength perspectives. As stated, γ-Ge_3N_4 and γ-Sn_3N_4 can be synthesized [13,14]. However, γ-Ge_3N_4 is a high pressure modification of the most stable phase of Ge_3N_4, *i.e.*, phenacite (p-Ge_3N_4) [3], while only γ-Sn_3N_4 is synthesized at ambient pressure.

Firstly, to gain deep insight into the stability of γ-$(Sn_{0.5}Ge_{0.5})_3N_4$, the enthalpy of formation (ΔH_f) has been calculated from a) its constituent elements ($\Delta H_{f,elements}$), b) γ-Ge_3N_4 and γ-Sn_3N_4 ($\Delta H_{f,spinel-spinel}$), and c) p-$Ge_3N_4$ (phenacite) and γ-Sn_3N_4 ($\Delta H_{f,phenacite-spinel}$). $\Delta H_{f,elements}$ / $\Delta H_{f,spinel-spinel}$ / $\Delta H_{f,phenacite-spinel}$ measures the change in enthalpy upon forming a compound from its constituent elements in their standard states / γ-Ge_3N_4 and γ-Sn_3N_4 / p-Ge_3N_4 and γ-Sn_3N_4; therefore it can be directly obtained from the total energies as follows [81,82]:

$$\Delta H_{f,elements}[\gamma-(Sn_{0.5}Ge_{0.5})_3N_4)] = E_{tot}[\gamma-(Sn_{0.5}Ge_{0.5})_3N_4)] - \left\{4\cdot\mu_N{}^0 + 3\cdot\left[0.5\cdot\mu_{Sn}{}^0 + 0.5\cdot\mu_{Ge}{}^0\right]\right\} \quad (1)$$

$$\Delta H_{f,spinel-spinel}[\gamma-(Sn_{0.5}Ge_{0.5})_3N_4)] = E_{tot}[\gamma-(Sn_{0.5}Ge_{0.5})_3N_4)] - 1/2\{E_{tot}[\gamma-Ge_3N_4] + E_{tot}[\gamma-Sn_3N_4]\} \quad (2)$$

$$\Delta H_{f,phenacite-spinel}[\gamma-(Sn_{0.5}Ge_{0.5})_3N_4)] = E_{tot}[\gamma-(Sn_{0.5}Ge_{0.5})_3N_4)] - 1/2\{E_{tot}[p-Ge_3N_4] + E_{tot}[\gamma-Sn_3N_4]\} \quad (3)$$

where E_{tot}[γ-$(Sn_{0.5}Ge_{0.5})_3N_4$)], E_{tot}[p-Ge_3N_4)], E_{tot}[γ-Ge_3N_4]and E_{tot}[γ-Sn_3N_4] are the total energy per formula unit of γ-$(Sn_{0.5}Ge_{0.5})_3N_4$)], p-Ge_3N_4, γ-Ge_3N_4 and γ-Sn_3N_4; $\mu_i{}^0$ (i = N, Ge, Sn) are the total energies per atom of the constituent elements in their elemental reference phase (see Table S3). Enthalpies here calculated provide an energy scale that measure the strength of

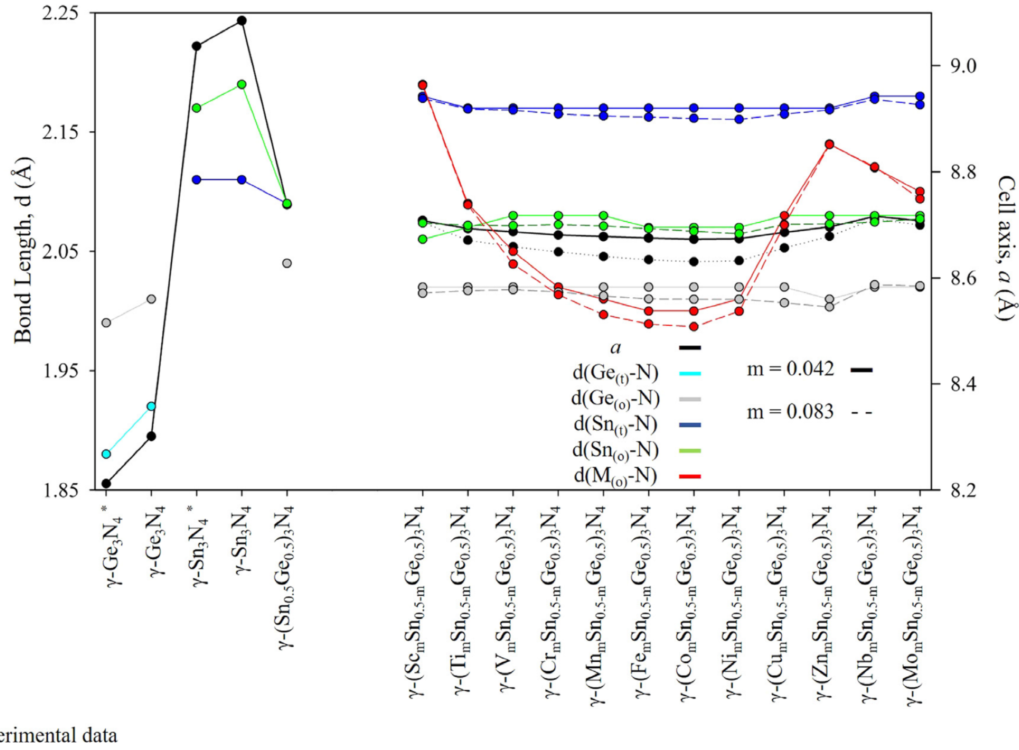

Fig. 2. Lattice parameters (a) and average bond distances (d) obtained for optimized crystal structure of γ-$(Sn_xGe_{1-x})_3N_4$ (x = 0.0, 0.5, 1.0) and γ-$(M_mSn_{0.5}Ge_{0.5})_3N_4$ (m = 0.042, 0.083). Units are in Angstroms (Å). For more details, see Fig. 1 and Tables S1 and S2 in the Supplementary Material. Experimental data taken from references [11,78].

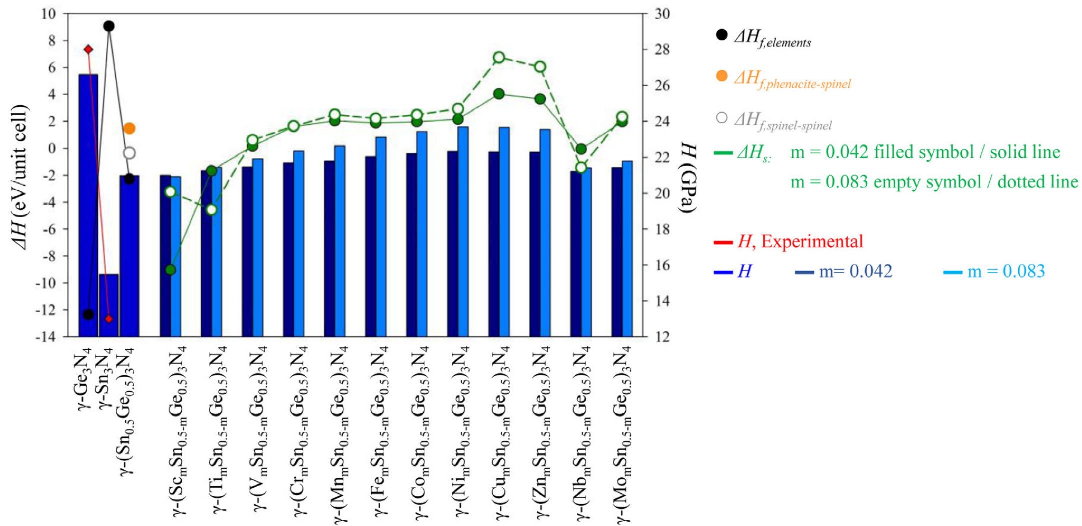

Fig. 3. The calculated enthalpies of formation (ΔH_f) and substitution (ΔH_s) and Hardness (H) values for γ-$(Sn_xGe_{1-x})_3N_4$ (x = 0.0, 0.5, 1.0) and γ-$(M_mSn_{0.5-m}Ge_{0.5})_3N_4$ (m = 0.042, 0.083). Experimental Hardness data taken from reference [83].

chemical bonding in a compound relative to the strength of bonding in its constituents (for $\Delta H_{f,elements}$) or respect to a reference compound ($\Delta H_{f,spinel\text{-}spniel}$ and $\Delta H_{f,phenacite\text{-}spinel}$).

In general, a negative ΔH_f determines ranges of chemical potentials of its constituents (elements in their elemental reference phase, γ-Ge_3N_4 and γ-Sn_3N_4 or p-Ge_3N_4 and γ-Sn_3N_4) within which the studied compound is thermodynamically stable [81]. As seen in Fig. 3, the lowest $\Delta H_{f,elements}$ (−16.56 eV/unit cell) is obtained for p-Ge_3N_4, while γ-Ge_3N_4 leads to $\Delta H_{f,elements}$ = −12.35 eV/unit cell. This trend agrees with experimental data, which points out to the larger stability of p-Ge_3N_4 phase. The fact that γ-Sn_3N_4 presents the highest formation enthalpy of all compounds (9.07 eV/unit cell) and it has been already synthetized suggest that $\Delta H_{f,elements}$ should not be considered as an insurmountable limitation of stability. The host material γ-$(Sn_{0.5}Ge_{0.5})_3N_4$ presents a negative value (−2.28 eV/unit

cell), not much higher than γ-Ge_3N_4 (−12.35 eV/unit cell), the most stable compound with spinel structure. Anyway, a low value of $\Delta H_{f,phenacite\text{-}spinel}$ along to a negative $\Delta H_{f,spinel\text{-}spinel}$ suggest that γ-$(Sn_{0.5}Ge_{0.5})_3N_4$ spinel would be relatively more stable than γ-Sn_3N_4. Though the host γ-$(Sn_{0.5}Ge_{0.5})_3N_4$ spinel could be stable, it could be not easily synthesizable, and may require some genuine chemistry methods such as pressure or templating.

Then, starting with the ternary γ-$(Sn_{0.5}Ge_{0.5})_3N_4$ spinel as reference, the enthalpy of substitution (ΔH_s) of M-hyperdoped spinels has been calculated as:

$$\Delta H_s[\gamma - (M_m Sn_{0.5-m} Ge_{0.5})_3 N_4] = \left\{E_{tot}[\gamma - (M_m Sn_{0.5-m} Ge_{0.5})_3 N_4] + 3m \cdot \mu_{Sn}{}^0\right\} - \left\{E_{tot}[\gamma - (Sn_{0.5} Ge_{0.5})_3 N_4] + 3m \cdot \mu_M{}^0\right\} \quad (4)$$

where $E_{tot}[\gamma\text{-}(M_mSn_{0.5\text{-}m}Ge_{0.5})_3N_4]$ and $E_{tot}[\gamma\text{-}(Sn_{0.5\text{-}m}Ge_{0.5})_3N_4]$ are the total energy per formula unit of γ-$(M_mSn_{0.5\text{-}m}Ge_{0.5})_3N_4$ and γ-$(Sn_{0.5\text{-}m}Ge_{0.5})_3N_4$; $\mu_i{}^0$ (i = Sn, M) are the total energies per atom of the constituent elements in their elemental reference phase (see Table S3). The trend of ΔH_s upon $Sn_{(o)}$ replacement by a transition metal can be related to the stability of γ-$(M_mSn_{0.5\text{-}m}Ge_{0.5})_3N_4$ respect to γ-$(Sn_{0.5}Ge_{0.5})_3N_4$. The lowest ΔH_s are obtained for M = Sc, Ti and Nb. For M = V, Cr, Mn, Fe, Co, Ni and Mo at the lowest m concentration, ΔH_s lie between 0 and 2 eV/unit cell. These values are slightly larger (by ~ 0.05 eV/atom) than the formation enthalpy of the host material. Finally, M = Cu and Zn hyperdoping lead to the highest ΔH_s. Regarding M concentration, ΔH_s tends to decrease along with M quantity, although similar conclusions are obtained despite the concentration.

The bonding strength has been studied through the intrinsic hardness (from now on, hardness, H), which is defined as an isotropic quantity that defines the resistance of a material to bond breaking [84,85]. Note that this definition entails a single fundamental quantity which does not necessarily equal the measured hardness [84,85]. The hardness has been calculated from the bond strengths (S) of the tetrahedral and octahedral bonds (S_{AN} and S_{BN}). See the Supplementary material for a more detailed description on the approach here used to obtain Hardness values. As seen, both enthalpies and intrinsic hardness properties are closely related through the bond strength

The calculated H values are collected in Fig. 3. For γ-Ge_3N_4 (H = 26.60 GPa) and γ-Sn_3N_4 (H = 15.46 GPa) our results are in good accordance with previous ones [84,85] and experimental data [83]. As expected γ-$(Sn_{0.5}Ge_{0.5})_3N_4$ presents an intermediate hardness value (H = 20.98 GPa) between H values for γ-Ge_3N_4 and γ-Sn_3N_4. The binary nitride γ-Ge_3N_4 is the hardest material, while the H decreases with the Sn proportion. Such trend can be explained based on smaller atomic radii of Ge atom (1.39 Å) respect to Sn (1.58 Å) and higher d(Sn-N) distances. Both factors lead to higher bond strengths and, hence, higher H values. H values for M-hyperdoped compounds lie between H = 22.30 GPa (M = Ni, m = 0.083) and H = 20.88 GPa (M = Cu, m = 0.042), which entails variations ≤ 6% respect to the ternary nitride γ-$(Sn_{0.5}Ge_{0.5})_3N_4$. In general, larger M concentrations leads to higher H values. Ni-hyperdoped spinel yields the highest hardness with R_i = 1.25 Å for Ni atom, d($Ni_{(o)}$-N) ~ 2.01 Å and a higher electronic valence charge of Ni (*Z: $3d^84s^2$*) respect to Sn (*Z: $5s^25p^2$*), which entails higher $S_{Ni(o)N}$ contribution respect to $S_{Sn(o)N}$.

3.2. Electronic band structure and optical absorption features of the host semiconductor γ-$(Sn_{0.5}Ge_{0.5})_3N_4$

Electronic band structures of γ-Ge_3N_4 and γ-Sn_3N_4 have been extensively studied by using *ab-initio* methods [3,18,19,21–23]. However, only the bandgap value (E_g ≃ 2.2 eV, calculated by DFT using the MBJ functional) has been reported for the ternary nitride compound γ-$(Sn_{0.5}Ge_{0.5})_3N_4$ [18]. Fig. 4a) shows the electronic band structure of γ-$(Sn_xGe_{1\text{-}x})_3N_4$ (x = 0.0, 0.5, 1.0) calculated within sc-GW_0. In addition, main results derived from DFT results obtained with PBE functional are also given (see Fig. S2) because *i)* PBE eigenvalues are used as starting point for sc-GW_0 and *ii)* they provide a more detailed information about atomic band composition or effective masses, otherwise unaffordable due to the high computational cost of sc-GW_0. As seen in Fig. S2, both PBE and sc-GW_0 methods give similar qualitative electron band structure patterns. However, accurate methods (*sc-GW_0*) are need for a quantitative description of the energy levels.

Our results for γ-Ge_3N_4 and γ-Sn_3N_4 are in agreement with previous *ab-initio* reported data [3,18,19,21–23] as well as with experimental ones [12,18,33]. Both γ-Ge_3N_4 and γ-Sn_3N_4 exhibit a direct bandgap (3.17 eV and 1.38 eV, respectively), in which conduction band minimum (CBM) and valence band maximum (VBM) are located at the Γ-point. Even though, the energy of the highest valence band at Γ and M-points is almost the same. The upper valence bands of γ-Ge_3N_4 / γ-Sn_3N_4 are mainly due to N-p states (as well as $Ge_{(o)}$-p / $Sn_{(o)}$-p orbitals in less extension), while the lower conduction bands are mainly due to N-p and $Ge_{(o)}$-s / $Sn_{(o)}$-s orbitals. $Sn_{(t)}$ and $Ge_{(t)}$ states appear at deep / high valence / conduction bands. As Figs. 4 and S2 show, the uppermost part of the VB in both systems is nearly flat (*i.e.*, high hole effective masses). This is most pronounced in γ-Sn_3N_4 and forms the basis for its reported short hole diffusion length [12,18]. The bottom of the CB, however, shows considerable dispersion (*i.e.*, low electron effective masses). The effective masses for holes and electrons have been calculated by a parabolic fitting of the VB and the CB along the directions Γ-R ($m^+{}_{\Gamma R}$ and $m^-{}_{\Gamma R}$, respectively) Γ-M ($m^+{}_{\Gamma M}$ and $m^-{}_{\Gamma M}$) and Γ-X ($m^+{}_{\Gamma X}$ and $m^-{}_{\Gamma X}$), while the average total effective mass (m^+ and m^-) due to multiple band maxima or minima has been defined to the sum of the inverse of the individual masses as follows:

$$m^* = \frac{3}{\frac{1}{m^*{}_{\Gamma R}} + \frac{1}{m^*{}_{\Gamma M}} + \frac{1}{m^*{}_{\Gamma X}}} \quad (4)$$

We found that m^+/m^- = 0.10 / 0.21 and m^+/m^- = 1.08 / 0.11 for γ-Ge_3N_4 and γ-Sn_3N_4, respectively (see Fig. 4b and Table S6). Larger m^+ values of γ-Sn_3N_4 agree with short hole diffusion lengths. The electronic band structure of γ-$(Sn_{0.5}Ge_{0.5})_3N_4$ can be described as an intermediate situation between both γ-Ge_3N_4 and γ-Sn_3N_4 extrema. When increasing the quantity of Sn, the VB goes upward while the CB slightly moves downward, resulting in a direct bandgap value E_g = 2.00 eV. In agreement to Caskey et al.,[12] the alloying between Ge and Sn in ternary nitrides leads to lower hole effective mass (m^+ = 0.73 for γ-$(Sn_{0.5}Ge_{0.5})_3N_4$), while electron effective mass remains unaffected.

3.3. Electronic band structure properties of γ-$(M_mSn_{0.5\text{-}m}Ge_{0.5})_3N_4$: seeking the most suitable transition metals to obtain an IGB-material

The substitutional hyperdoping of $Sn_{(o)}$ by transition metals has been proposed here to obtain an in-gap-band material. This strategy is based on: *(i)* the well-known ability of d-orbitals of transition metals to be located within the bandgap of the host material allowing the formation of an isolated energy band; *(ii)* cations in an octahedral environment ($Ge_{(o)}$ and $Sn_{(o)}$) and N provide the main contribution to the band edges of γ-$(Sn_{0.5}Ge_{0.5})_3N_4$; *(iii)* almost all transition metals tend to present an octahedral coordination; [86] *(iv)* the bond strength order ($S_{Sn(t)}$ = 2.25 > $S_{Ge(o)}$ = 0.36 > $S_{Sn(o)}$ = 0.33) points out that the replacement of a $Sn_{(o)}$ atom by M would be more favored than the substitution of $Ge_{(o)}$.

Figs. S3-S14 display electronic band structure and Projected Density of States (PDOS) of γ-$(M_mSn_{0.5\text{-}m}Ge_{0.5})_3N_4$. Once again, both PBE and sc-GW_0 yield similar qualitative band structures and

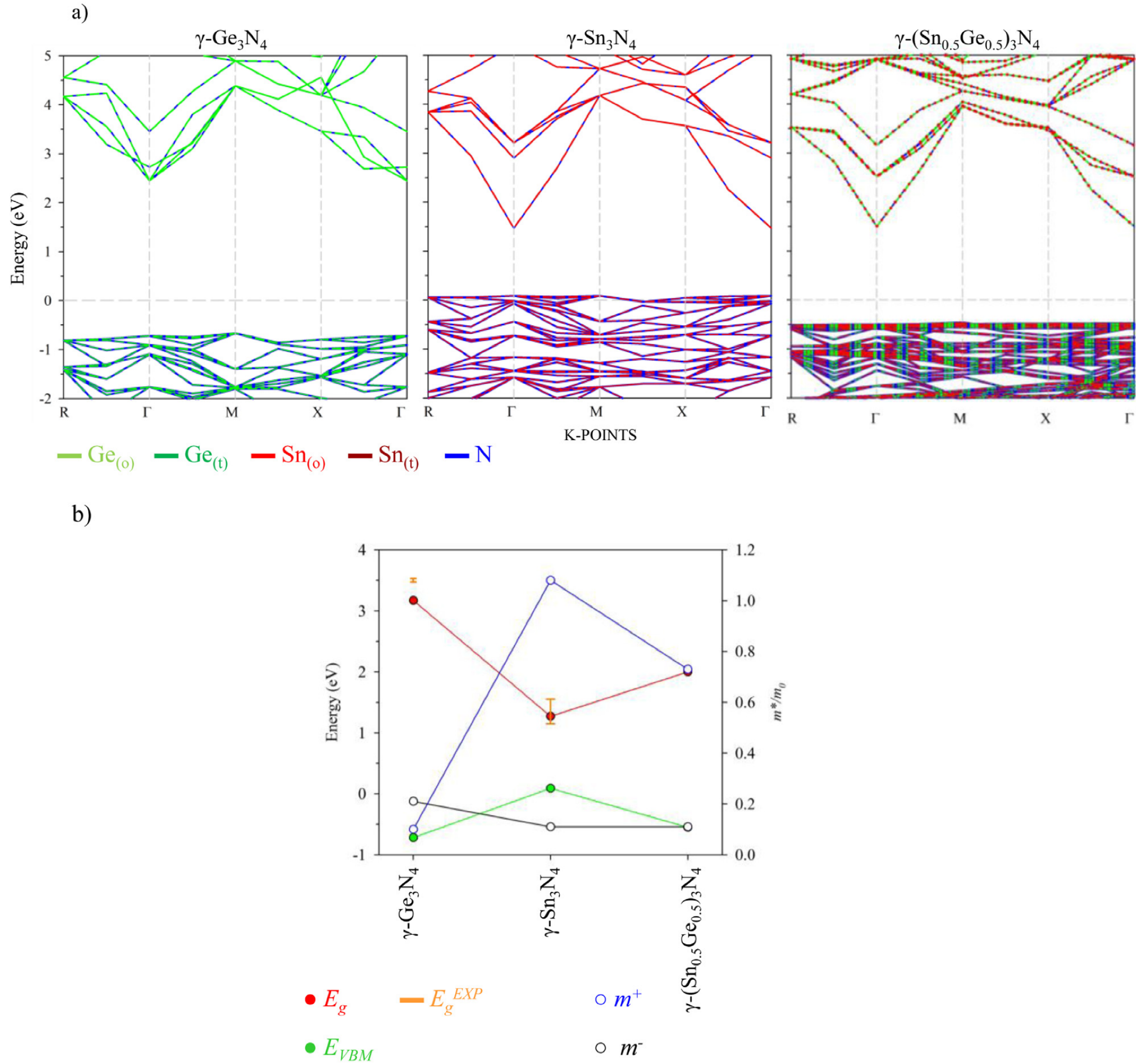

Fig. 4. a) Projected electronic band structure (only the main atomic contributions have been qualitatively considered) of γ-$(Sn_xGe_{1-x})_3N_4$ (x = 0.0, 0.5, 1.0) calculated within the sc-GW_0 approach. The zero energy has been set at the Fermi level (gray dotted line). For a more detailed description of electronic bands compositions, Fig. S2 displays the projected density of states; b) Summary of the main electronic structure band parameters: bandgap (E_g), position of the VBM respect to the Fermi level (E_{VBM}) and effective masses for holes (m^+) and electrons (m^-). Experimental bandgap values taken from references [12,18,33].

density of states patterns near the band edges as well as for those new states appearing within the bandgap of the host material. Hence, information about the nature of electronic states has been obtained from PBE, while sc-GW_0 is needed for an accurate description of energy levels. As seen previously for the host material, the VB (CB) is mainly dominated by N-p and $Ge_{(o)}$-p and $Sn_{(o)}$- p (N-p and $Ge_{(o)}$-s and $Sn_{(o)}$-s) orbitals. Electronic structure changes upon M-hyperdoping could be described as a direct consequence of the crystal field created by N atoms around M ones [86,87], and the electronic filling of d-levels. Fig. 5 shows a scheme of the splitting and electron filling scheme of transition metal d-orbitals in γ-$(M_mSn_{0.5-m}Ge_{0.5})_3N_4$. In the octahedral geometry, the six N atoms are oriented along the longitudinal z-axis and the diagonal directions of the xy plane. In the crystal field theory, the interaction between the transition metal and N atoms would cause a split of M-3d orbitals into a low-energy t_{2g} triplet (due to d_{xy}, d_{xz} and d_{yz}) and a high-energy e_g doublet (d_{z^2} and $d_{x^2-y^2}$). These levels further split into spin-up and spin-down components. For M=V, Cr, Fe, Co, Nb and Mo there is a compression of the octahedra along the longitudinal z-axis, which leads to a non-degenerated t_{2g} triplet [88]. For M-hyperdoped spinels (M = Fe, Co, Ni, Cu), two (high or low) spin configurations would be possible. As seen in Fig. 5, M-hyperdoping (M = Fe, Co, Ni, Cu) always leads to a low-spin configuration for M-hyperdoped spinels. This tendency is related to strong crystal coordination fields around M.

Fig. 6 collects bandgap values obtained within sc-GW_0 approach measured at Γ-point. Based on bandgap values, γ-$(M_mSn_{0.5-m}Ge_{0.5})_3N_4$ can be grouped in three families of semiconductor materials:

a) M-hyperdoped spinels with a single gap (M = Sc, Ti, Mn, Ni, Nb). This family includes those semiconductors with a single gap due to VB - CB energy difference for those bands belonging to the host semiconductor. Except for M = Mn, these spinels yields a bandgap ~ 2.0 eV (E_g of the host material).

			m = 0.042		m = 0.083	
M	Z	*D*	Spin Up	Spin Down	Spin Up	Spin Down
Sc	$3d^14s^2$	0				
Ti	$3d^24s^2$	0				
V	$3d^34s^2$	1				
Cr	$3d^54s^1$	2				
Mn	$3d^54s^2$	3				
Fe	$3d^64s^2$	4				
Co	$3d^74s^2$	5				
Ni	$3d^84s^2$	6				
Cu	$3d^{10}4s^1$	7				
Zn	$3d^{10}4s^2$	8				
Nb	$4d^45s^1$	1				
Mo	$4d^55s^1$	2				

Fig. 5. Schematic representation of the splitting of *d*-orbitals in an octahedral coordination for γ-$(M_mSn_{0.5-m}Ge_{0.5})_3N_4$. The valence electronic configuration (*Z*) of M and the number of extra electrons (*D*) respect to Sn (*Z*: $5s^25p^2$) are also shown. Energy levels are qualitatively located respect to the Fermi level (grey dotted lines). Blue and orange lines stand for the VMB and CBM. For a more detailed description, see Figs. S3–S14.

b) M-hyperdoped spinels with a pseudo-in-gap-band (M=V, Fe, Zn, Mo). A pseudo-in-gap-band (pseudo-IGB) has been here defined as a band located inside the gap of the host semiconductor, which meets some requirements to be defined as an IGB: *(i)* have its own small dispersion, without being at a discrete level; *(ii)* be well isolated from the band edges. However, this *pseudo*-IGB is not partially filled. In addition to VB → CB transitions belonging to the host material, these semiconductors would only allow an extra sub-bandgap VB → *pseudo*-IGB or *pseudo*-IGB → CB transition for filled or empty *pseudo*-IGB, respectively.

c) M-hyperdoped spinels with an in-gap-band (M =Cr, Co, Cu). The hyperdoping with M leads to a new level in the host semiconductor bandgap which mainly comprises M-3d orbitals. These new levels fulfill the requirements to play as IGB, *i.e.*, this band is partially filed (the Fermi level crosses it), well isolated from both VB and CB and has a small dispersion. Therefore, new optical sub-bandgap transitions across the IGB (VB → IGB and IGB → CB) could be also expected.

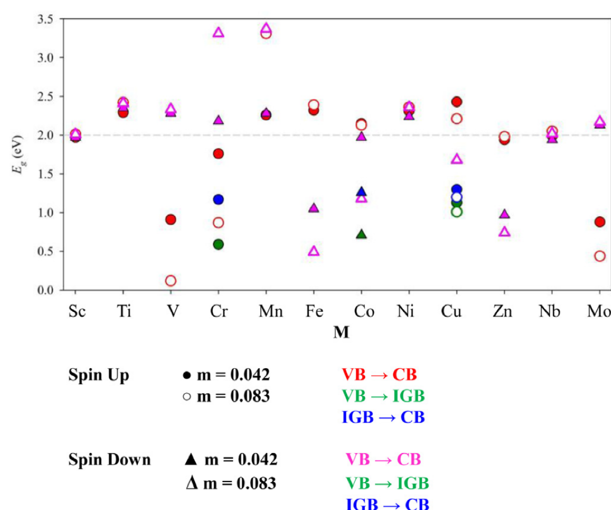

Fig. 6. Bandgap values (E_g) for γ-$(M_mSn_{0.5\text{-}m}Ge_{0.5})_3N_4$ calculated within sc-GW_0 approach measured at Γ-point. Dashed horizontal lines stands for γ-$(Sn_{0.5\text{-}m}Ge_{0.5})_3N_4$. For more details, see Table S7.

Because this paper is devoted to spinel-type nitride compounds with an IGB as efficient sunlight absorbers, results and discussions regarding the electronic structure of families *a)* and *b)* have been moved to the Supplementary material for the sake of clarity.

Fig. 7 displays the electronic band structure of M-hyperdoped spinels (M = Cr, Co, Cu; $m = 0.042$), where the substitutional doping with M leads to the formation of an IGB calculated with *sc-GW₀*. Starting from the Cr (Z: $3d^54s^1$) and Sn (Z: $4s^24p^2$) shell configuration, for spin-up the t_{2g} triplet allocates the two extra electrons, while the e_g doublet would be empty. Because of the compression of the octahedra around the Cr atom along the longitudinal axis, the t_{2g} levels are not degenerated. Thus, the low energy d_{xy} orbital is full with one electron defining the last occupied valence band, whilst degenerated d_{xz} and d_{yz} states are semi-filled with one electron forming an IGB. This IGB is well isolated from both the CB and VB, with an energy difference equal to 1.17 eV / 0.59 eV at Γ-point. The energy difference between the IGB and the lowest occupied / highest valence band leads to a bandgap of 1.76 eV. However, the bandgap of the host materials (measured as the energy difference between VB and CB belonging to the host spinel) is opened to 2.18 eV at Γ-point. The high energy e_g doublet appears at much high energy mixed with high energy conduction bands. For spin-down channel, Cr-hyperdoped spinel yields a semiconductor band structure pattern with a (nearly) direct band-gap at Γ-point, which is opened to 2.18 eV (*i.e.*, 0.18 eV with respect to the host material). Rigorously speaking, this material owns a nearly direct bandgap at Γ-point, while the indirect bandgap is measured at M-Γ points (see Table S7) due to non-degenerated energies of the highest valence band at Γ and M points. This fact is also noted for M = Co, Cu. Since the differences between direct and indirect bands are ≤ 0.15 eV, from now on will we be focused on the nearly direct bandgap at Γ.

The substitutional hyperdoping with M = Co (Z: $3d^74s^2$) leads to a low-spin configuration for the transition metal. For the spin-up channel, Co-hyperdoped spinel shows a direct gap $E_g = 2.15$ eV at Γ-point. This gap is due to the energy difference between occupied and excited states belonging to the host material. Meanwhile, the t_{2g} manifold (which is filled with three electrons) appears at deeper energies mixed with deep valence bands and the e_g doublet is located at 0.69 eV (Γ-point) over the CBM. For the spin-down component, Co-hyperdoped spinel meets the requirements to play as in-gap-band material. Due to the longitudinal compression along z-axis, one t_{2g} state appears overlapping the VB at Γ and M-points, this level defines the highest valence band. Thus, the IGB is due to the remaining t_{2g} levels, that are semi-filled with one electron (see Fig. 5). This IGB is well differentiated from both VB (VB-IGB energy difference = 0.71 eV at Γ-point) and CB (IGB-CB energy difference equal to 1.26 eV at Γ-point). The VB-CB energy gap is 1.97 eV (slightly lower than the bandgap of the host material). High-energy e_g doublet is observed ~ 2.21 eV over the Fermi energy. Thus, the crystal-field splitting energy separating the t_{2g} and e_g states is estimated to be ~ 2.21–2.82 eV at Γ.

Substitutional doping with Cu (Z: $3d^{10}4s^1$) also leads to a low-spin configuration for the transition metal. For spin-up component, new isolated energy levels appear in the gap of the host semiconductor around the Fermi level due to high energy e_g doublet of Cu. Note that this e_g doublet is semi-filled with one electron leading to a IGB (see Fig. 5), while the low energy t_{2g} triplet appears at much lower energy mixed with the valence bands belonging to the host spinel. As seen in Fig. 7, the in-gap-band is well differentiated from the band edges (the energy difference between the IGB and the VB/CB is 1.07 eV / 1.30 eV at Γ-point). Hence, the bandgap of the host material increases to 2.37 eV at Γ-point. For spin-down channel, Cu hyperdoping leads to an electronic band structure with an empty *pseudo*-IGB band. The gap of the system, defined as the energy difference between the VB belonging to the host spinel and the *pseudo*-IGB, is 1.69 eV, while the energy gap for the host material is 2.11 eV.

As discussed, the formation of an IGB can be explained based on the crystal field theory. However, a detailed inspection of the projected density of states for M = Cr and Co (Fig. 8a) shows that both the IGB and the highest valence band comprise a mix of d_{xy}, d_{xz} and d_{yz} states. This mixing between different 3*d* levels leading to the IGB is mainly due to the axial compression of the octahedral void around the transition metal. As expected, the IGB for M = Cu is mainly due to d_{z^2} and $d_{x^2-y^2}$.

In addition to be narrow enough to be well isolated from the valence and conduction band edges of the host semiconductor, the IGB must own small dispersion without being a discrete level. As seen in Fig. 7, the formed in-gap bands own small dispersion, whose largest bandwidths lie between 0.11 eV (M = Co) and 0.43 eV (for M = Cu). For M = Co and Cu, the wavefunction of the IGB states overlaps with the interacting orbitals of the neighboring atoms, which agrees with a non-localized defect state. However for M = Cr, the partial charge density for the IGB is mainly concentrated around the transition metal (see Fig. 8b).

The influence of M concentrations on the electronic structure has also been assessed. At higher M concentrations ($m = 0.083$), for M = Cr (Figs. 5, 6 and S6), the electronic band structure for spin-up component shows two pseudo-IGB bands coming from Cr-3d levels. The energy gap (0.87 eV at Γ-point) is due to the energy difference between both pseudo-IGB, while the bandgap of the host-spinel is opened to 2.92 eV. For M = Co (Fig. 5, 6 and S9), the IGB increases its bandwidth due to higher m values. Thus, there is an overlap between Co-*3d* states and the valence band belonging to the host material. The gap of the system due to the energy difference between the CB and filled Co-*3d* states is $E_g = 1.18$ eV at Γ-point. The formation of an intermediate band needs high concentration of IGB states (above the Mott Limit: $5{\bullet}10^{19}$ cm^{-3}) to produce both high absorption coefficient and to avoid non radiative recombination. Therefore, M concentrations between $5{\bullet}10^{19}$ cm^{-3} and $1.5{\bullet}10^{21}$ cm^{-3} ($m = 0.042$) would be adequate to form an in-gap-band through the hyperdoping with M = Cr, Co, while M concentrations higher than $2.9{\bullet}10^{21}$ cm^{-3} ($m = 0.083$) would entail the no-formation of an IGB. For M = Cu, an IGB is also formed at higher m values (see Figs. 5, 6 and S11), whose features are only slightly changed upon m increase. Thus, the main energy differ-

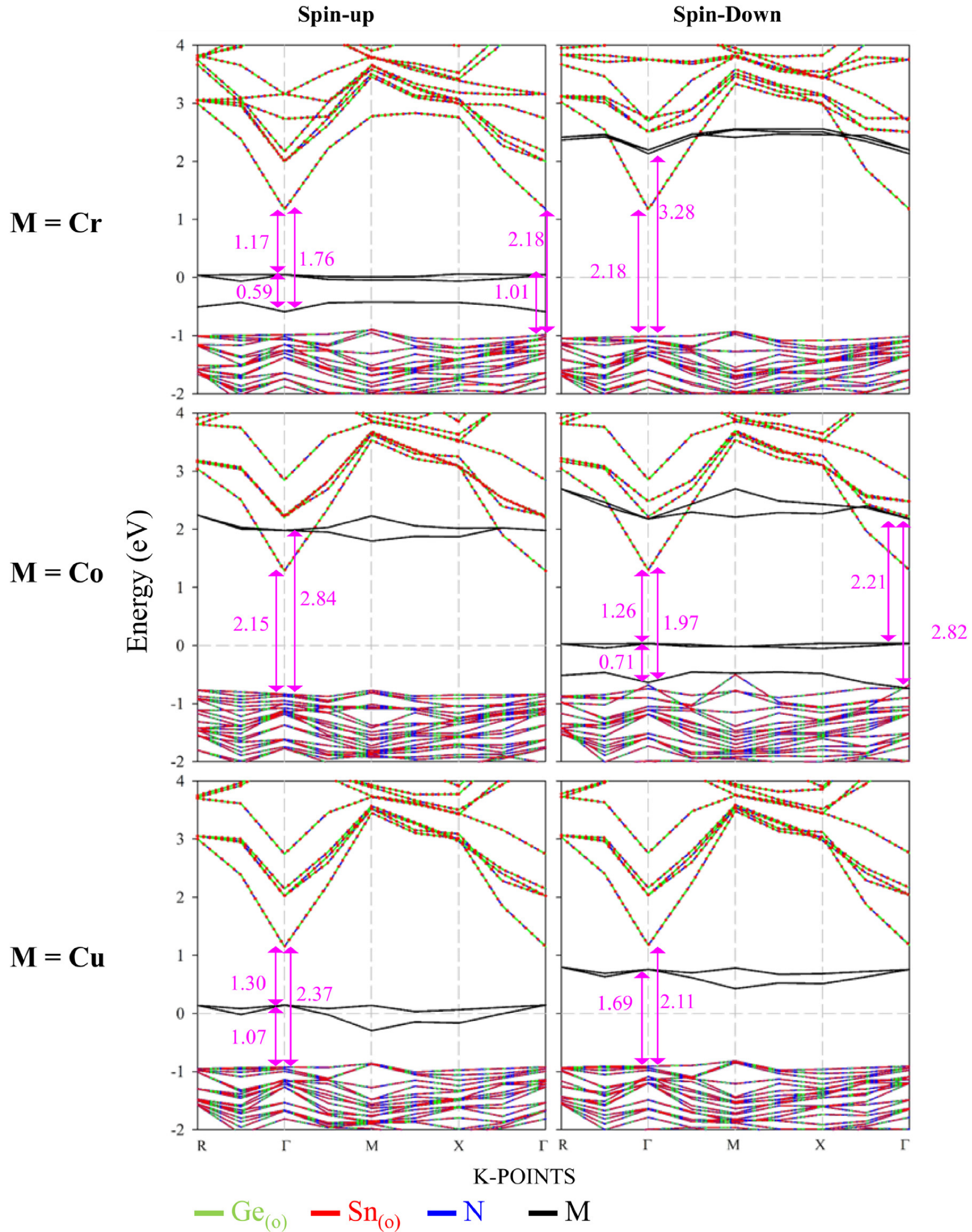

Fig. 7. Projected electronic band structure (only the main atomic contributions have been considered) of γ-$(M_mSn_{0.5\text{-}m}Ge_{0.5})_3N_4$ (m = 0.042; M = Cr, Co, Cu) calculated within sc-GW_0 approach. The zero energy has been set at the Fermi level (gray dotted line); vertical arrows stands for the main energy differences measured at Γ-point.

ences are 1.01/ 1.20 / 2.21 eV for VB - IGB / IGB-CB / VB-CB at Γ-point.

3.4. Absorption features and photovoltaic efficiency of in-gap-band materials

Optical absorption features and photovoltaic efficiency of M-hyperdoped spinels with an IGB (M = Cr, Co, Cu) have been assessed. Because the in-gap formation depends on the M concentration, absorption properties and photovoltaic efficiencies here discussed are only referred to m = 0.042. Fig. 9a shows the absorption coefficient for γ-$(Sn_{0.5}Ge_{0.5})_3N_4$ and γ-$(M_mSn_{0.5\text{-}m}Ge_{0.5\text{-}m})_3N_4$ ((M = Cr, Co and Cu; m = 0.042). Solar spectrum is also presented in the background. As expected, in the case of the host γ-$(Sn_{0.5}Ge_{0.5})_3N_4$ the absorption edge starts at ~ 2.0 eV, which corresponds with the bandgap of the host material. Hyperdoping with M = Cr, Co, Cu leads to an improvement in the absorption features below the bandgap of the host material. As seen in Fig. 9a,

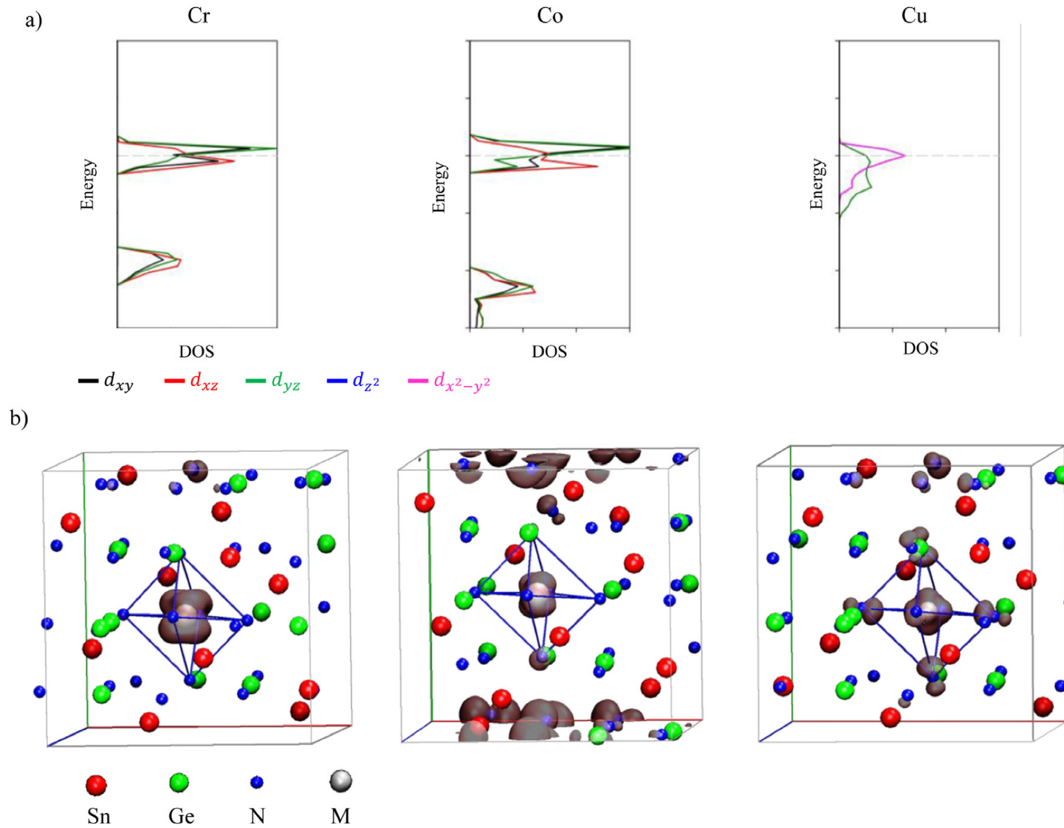

Fig. 8. **a**) Projected density of states of γ-$(M_mSn_{0.5\text{-}m}Ge_{0.5})_3N_4$ (m = 0.042; M = Cr, Co, Cu) showing the contribution of M *3d*-orbitals forming the IGB. The zero energy was set at the Fermi level (black dotted line); **b**) the partial charge density isosurfaces (displayed at 10% of their maximum value) of the in-gap-band states for γ-$(M_mSn_{0.5\text{-}m}Ge_{0.5})_3N_4$ (m = 0.042; *M* = Cr, Co, Cu). Octahedral environment around M atom is also displayed.

the absorption is extended up to 0.5 eV. But, the gained photon-absorption is not only noted below 2.0 eV, also for energies higher than the bandgap of γ-$(Sn_{0.5}Ge_{0.5})_3N_4$.

Aimed at quantifying the role of the transition metal in the absorption enhancements of M-hyperdoped spinels, the absorption coefficient has been decomposed as a sum of the independent VB →IGB, IGB → CB and VB →CB transitions. The existence and location of overlapping and hidden peaks are found by data differentiation. Thus, the analysis of the second and fourth derivatives of the absorption coefficient has revealed the presence of hidden and overlapped peaks. Then, the absorption coefficient has been deconvolved by fitting a set of Gaussian peaks to the calculated absorption coefficient. Obtained peaks were assigned based on their energies in comparison to energy differences measured in the electronic band structure. Finally, those transitions corresponding to the same type have been grouped under the same curve: VB →IGB, IGB → CB and VB → CB. Decomposed absorption coefficients are presented in Fig. 9b. In addition, the area under the curve (*AUC*), which defines the integral of a curve that describes the absorption as a function of the energy, has been used as a quantitative measurement of the photo-absorption respect to the host material (see Fig. 10). Both analyses have been carried out between 0.5 and 2.5 eV, which covers the highest spectral irradiance of the Solar spectrum (see Fig. 9a). Absorption peaks below 0.5 eV are assigned to electronic transitions between the different states forming the IGB. Although these low-energy transitions slightly contribute to the overall absorption process, they are not directly related to the photocurrent generation of the device [63]. Results reflect well the enhancement of the absorption features, excepting the case of M = Cr which presents similar absorption rates than the host material (AUC = $1.87 \cdot 10^4$ cm^{-1} eV). For this material, there is loss of the photo-absorption of the host which is compensated due to new transitions across the IGB. M=Co shows significant increment (AUC = $2.52 \cdot 10^4$ cm^{-1} eV), while M=Cu exhibits a rise of more than 150% (AUC = $3.01 \cdot 10^4$ cm^{-1} eV) mainly due to VB → IGB / IGB → CB transitions. Although the AUC related to VB → CB always entails ~ 75–80% of the total one, this is considerably increased upon doping with M = Co and Cu.

Finally, optical results are used to evaluate the photovoltaic efficiency (η) of the proposed materials. Using the methodology proposed by Luque et al.[34], based on the detailed-balance model but making the assumption of non-overlapping absorptions, we have obtained maximum efficiencies under solar concentrations of 100 suns as a function of E_g and the energy of the sub-bandgap transitions across the IGB (*i.e.*, VB → IGB and -IGB → CB) measured at Γ-point. We are aware that the real photovoltaic efficiency also depends on several factors such as the architecture of the solar cells, the contacts, etc., which are out of the scope of this paper. Thus, the simplicity of the used model renders values that must be considered only as an ideal superior limit. Nevertheless, the maximum efficiency here calculated could be used as a criterium to evaluate the potential of a material as sunlight absorber. As expected, M-hyperdoped spinels achieves higher η values than the host material (η = 25%), which lie between η = 35% for M = Cr, Cu and η = 55% for M = Co. As seen, the efficiency of Co-hyperdoped spinels clearly exceed the limits of a single-gap solar cell.

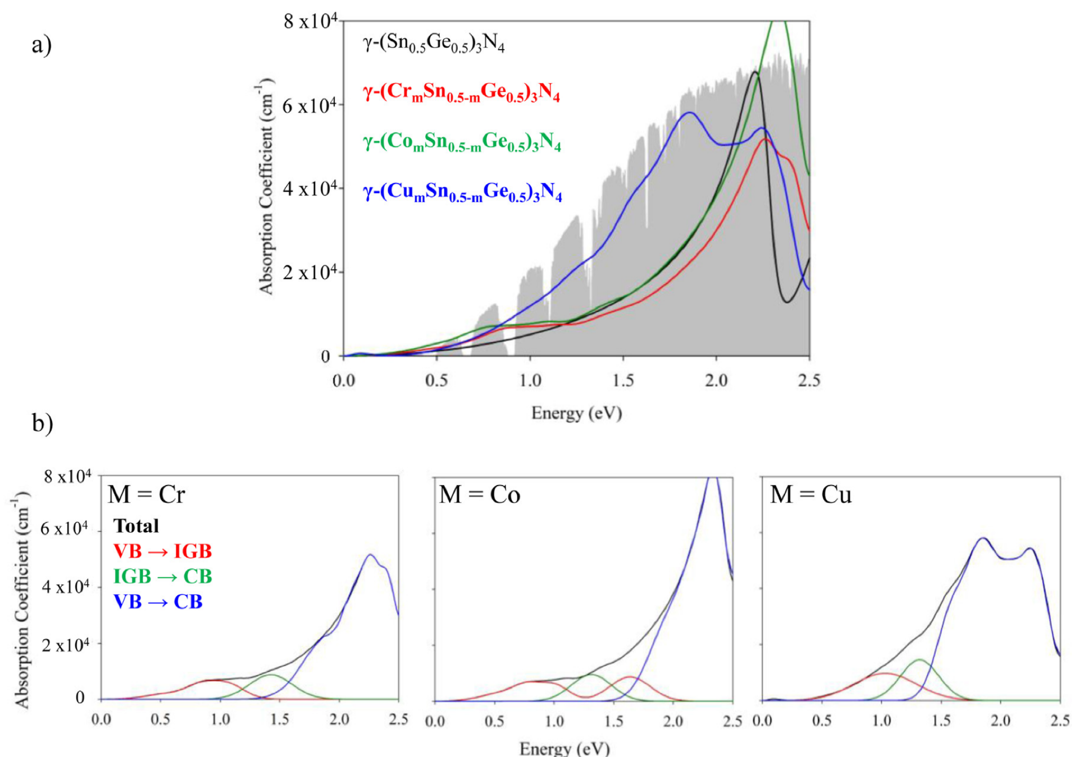

Fig. 9. a) Absorption coefficients for γ-($Sn_{0.5}Ge_{0.5}$)3 N and γ-($M_mSn_{0.5\text{-}m}Ge_{0.5}$)$_3N_4$ (m = 0.042; M = Cr, Co, Cu) spinels. The solar spectrum AM1.5G (in arbitrary units) has been included as a solid shape in background; b) Partial contributions to the Absorption Coefficients for γ-($M_mSn_{0.5\text{-}m}Ge_{0.5}$)$_3N_4$ (m = 0.042; M = Cr, Co, Cu) spinels.

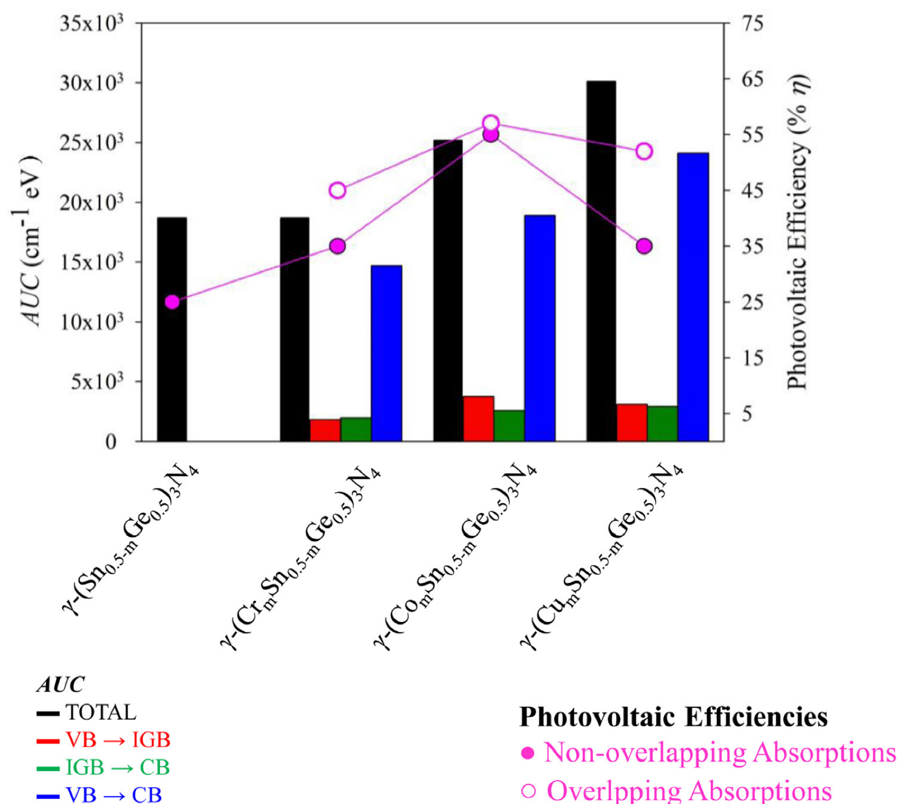

Fig. 10. Area under the curve (*AUC*) for the absorption coefficients along to detailed-balance maximum Photovoltaic Efficiency (% η) of γ-($Sn_{0.5}Ge_{0.5}$)$_3N_4$ and γ-($M_mSn_{0.5\text{-}m}Ge_{0.5}$)$_3N_4$ (M = Cr, Co, Cu; m = 0.042).

As seen in Fig. 9b, both VB → IGB and IGB → CB are overlapped as well as sharing photons. Although overlapping absorptions have generally been considered to be a source of losses. Krishna et al. proved that overlapping absorptions can lead to improved photovoltaic efficiencies [89]. Hence, the detailed-balance maximum photovoltaic efficiencies (% η) for a solar concentration of $X = 100$ has also been obtained for perfectly overlapping absorptions following the methodology proposed by Krishna et al. [89]. In this case, sub-bandgap and bandgap energies are measured at the highest values for the absorption coefficient which implies that the sum of VB → IGB and IGB → CB is larger than E_g. As seen in Fig. 10, the resulting photovoltaic efficiencies are higher in all the cases, where M = Cr, Cu increase their photovoltaic efficiencies up to η = 45% and 42% respectively, while for M=Co the efficiency presents a small increase up to η = 57%. Anyway, regardless of the approximation used, Co-hyperdoped spinel shows a considerable improvement with respect to the theoretical maximum conversion efficiency based on the SQ model.

4. Conclusions

By using accurate *ab-initio* methods, we assessed the potential of transition metal-hyperdoped IV-nitrides with spinel structure, with the general formula γ-$(M_mSn_{0.5\text{-}m}Ge_{0.5})_3N_4$ ($x = 0.5$; $m = 0.042, 0.083$), as efficient sunlight absorber materials to be used in photovoltaic devices. For this, we have systematic studied 3*d*-block elements (Sc, Ti, V, Cr, Mn, Fe, Co, Ni, Cu, Zn) along with the most abundant 4*d*-block ones (Nb, Mo) as dopant elements. All the results are summarized as follows:

- The stability of M-hyperdoped spinels were studied from both energetic and bonding strength perspectives. Calculated enthalpies of formation for the host material are below the upper limit defined by γ-Sn_3N_4. The bonding strength has been studied through the intrinsic hardness (*H*). *H* values for M-hyperdoped compounds entail variations ≤ 6% respect to the ternary nitride γ-$(Sn_{0.5}Ge_{0.5})_3N_4$. Both facts point that γ-$(Sn_{0.5}Ge_{0.5})_3N_4$ and γ-$(M_mSn_{0.5\text{-}m}Ge_{0.5})_3N_4$ could be stable.
- Changes in the electronic structure upon hyperdoping are explained based on the crystal field created by N atoms around M one and the electronic filling of *d*-levels. The substitutional hyperdoping with M= Cr, Co, Cu leads to the formation of an in-gap-band (IGB) in the gap of the host material with adequate properties to allow two extra photon-absorption process. A detailed analysis of the electronic structure shows that the degeneration breaking of t_{2g} manifold (due to the longitudinal compression of the octahedral around M) is key for the formation of such IGB, while this IGB is due to e_g doublet for Cu. It should be noted that Cr- and Co-hyperdoped shows similar stability (ΔH_f and *H*) features than the host material, while the largest deviations are obtained for M = Cu.
- Although electronic transitions across the bandgap of the host material (i.e., VB → CB) entail ~ 75% - 80% of the total photo-absorption, this is considerably improved due to electronic transitions across the IGB below the gap of the host spinel (i.e., VB → IGB and IGB → CB). The most adequate photo-absorption features are obtained for M = Co and Cu. The highest photovoltaic efficiency (η = 55–57%) is obtained for Co-hyperdoped spinel.

In short, our results point out that M-hyperdoped spinels, especially with M = Co, would be excellent candidates to be used in high-efficient photovoltaic devices as absorber material.

Declaration of Competing Interest

The authors declare that they have no known competing financial interests or personal relationships that could have appeared to influence the work reported in this paper.

Acknowledgments

This work was partially supported by the Ministerio de Economía y Competitividad through the project SEHTOP-QC (ENE2016-77798-C4-4-R) and by Universidad Politécnica de Madrid through the project DNSMEP (VJIDOCUPM19GGM). The authors gratefully acknowledge the Universidad Politécnica de Madrid (www.upm.es) for providing computing resources on Magerit Supercomputer. The statements made herein are solely the responsibility of the authors.

Supplementary materials

Supplementary material associated with this article can be found, in the online version, at doi:10.1016/j.actamat.2020.07.034.

References

[1] R.N. Katz, High-temperature structural ceramics, Science 208 (1980) 841 https://doi.org/10.1126/science.208.4446.841.
[2] G. Dufour, F. Rochet, H. Roulet, F. Sirotti, Contrasted behavior of Si(001) and Si(111) surfaces with respect to NH3 adsorption and thermal nitridation: a N 1s and Si 2p core level study with synchrotron radiation, Surf. Sci. 304 (1994) 33–47 https://doi.org/10.1016/0039-6028(94)90750-1.
[3] B. Molina, L.E. Sansores, Electronic structure of Ge3N4 possible structures, Int. J. Quantum Chem. 80 (2000) 249–257 https://doi.org/10.1002/1097-461X(2000)80:2<249::AID–QUA19>3.0.CO;2-9.
[4] A. Zerr, G. Miehe, G. Serghiou, M. Schwarz, E. Kroke, R. Riedel, H. Fueb, P. Kroll, R. Boehler, Synthesis of cubic silicon nitride, Nature 400 (1999) 340–342 https://doi.org/10.1038/22493.
[5] G. Serghiou, G. Miehe, O. Tschauner, A. Zerr, R. Boehler, Synthesis of a cubic Ge3N4 phase at high pressures and temperatures, J. Chem. Phys. 111 (1999) 4659–4662 https://doi.org/10.1063/1.479227.
[6] A. Zerr, R. Riedel, T. Sekine, J.E. Lowther, W.Y. Ching, I. Tanaka, Recent advances in new hard high-pressure nitrides, Adv. Mater. 18 (2006) 2933–2948 https://doi.org/10.1002/adma.200501872.
[7] S.-D. Mo, L. Ouyang, W.Y. Ching, I. Tanaka, Y. Koyama, R. Riedel, Interesting physical properties of the new spinel phase of Si_3N_4 and C_3N_4, Phys. Rev. Lett. 83 (1999) 5046–5049 https://doi.org/10.1103/PhysRevLett.83.5046.
[8] W.Y. Ching, S.-D. Mo, L. Ouyang, Electronic and optical properties of the cubic spinel phase of c-Si_3N_4, c-Ge_3N_4, c-$SiGe_2N_4$, c-$GeSi_2N_4$, Phys. Rev. B 63 (2001) 245110 https://doi.org/10.1103/PhysRevB.63.245110.
[9] W.Y. Ching, P. Rulis, Ab initio calculation of the electronic structure and spectroscopic properties of spinel γ-Sn_3N_4, Phys. Rev. B 73 (2006) 045202 https://doi.org/10.1103/PhysRevB.73.045202.
[10] J. Dong, O.F. Sankey, S.K. Deb, G. Wolf, P.F. McMillan, Theoretical study of β-Ge3N4 and its high-pressure spinel γ-phase, Phys. Rev. B 61 (2000) 11979 https://doi.org/10.1103/PhysRevB.61.11979.
[11] K. Leinenweber, M. O'Keeffe, M. Somayazulu, H. Hubert, P.F. McMillan, G.H. Wolf, Synthesis, structure refinement of the spinel, γ-Ge_3N_4, Chem. Eur. J. 5 (1999) 3076–3078, doi:10.1002/(SICI)1521-3765(19991001)5:10<3076::AID-CHEM3076>3.0.CO;2-D.
[12] C.M. Caskey, J.A. Seabold, V. Stevanovic, M. Ma, W.A. Smith, D.S. Ginley, N.R. Neale, R.M. Richards, S. Lany, A. Zakutayed, Semiconducting properties of spinel tin nitride, other IV3N4 polymorphs, J. Mater. Chem. C 3 (2015) 1389–1396 https://doi.org/10.1039/C4TC02528H.
[13] M. Zervos, A. Othonos, Enhanced growth and photoluminescence properties of SnxNy (x>y) nanowires grown by halide chemical vapor deposition, J. Cryst. Growth 316 (2011) 25–29 https://doi.org/10.1016/j.jcrysgro.2010.12.029.
[14] M. Huang, Y.P. Feng, Theoretical prediction of the structure and properties of Sn_3N_4, J. Appl. Phys. 96 (2004) 4015–4017 https://doi.org/10.1063/1.1788836.
[15] Y. Ding, H. Zhou, M. Xu, Y. Shen, Q. Chen, W.-J. Zhu, H. He, First-Principles study of gamma-Si_3N_4 with generalized gradient approximation and local density approximation, Int. J. Mod. Phys. B 22 (2008) 2157–2167 https://doi.org/10.1142/S0217979208039368.
[16] Y. Inoue, M. Nomiya, O. Takai, Physical properties of reactive sputtered tin-nitride thin films, Vacuum 51 (1998) 673–676 https://doi.org/10.1016/S0042-207X(98)00271-1.
[17] R.G. Gordon, D.M. Hoffman, U. Riaz, Low-temperature atmospheric pressure chemical vapor deposition of polycrystalline tin nitride thin films, Chem. Mater. 4 (1992) 68–71 https://doi.org/10.1021/cm00019a016.

[18] T.D. Boyko, A. Hunt, A. Zerr, A. Moewes, Electronic structure of spinel-type nitride compounds Si_3N_4, Ge_3N_4, Sn_3N_4 with tunable band gaps: application to light emitting diodes, Phys. Rev. Lett. 111 (2013) 097402 https://doi.org/10.1103/PhysRevLett.111.097402.
[19] I.-.H. Chu, A. Kozhevnikov, T.C. Schulthess, H.-.P. Cheng, All-electron GW quasi-particle band structures of group 14 nitride compounds, J. Chem. Phys. 141 (2014) 044709 https://doi.org/10.1063/1.4890325.
[20] S. Leitch, A. Moewes, L. Ouyang, W.Y. Ching, T. Sekine, Properties of non-equivalent sites and bandgap of spinel-phase silicon nitride, J. Phys. 16 (2004) 6469–6476 https://doi.org/10.1088/0953-8984/16/36/012.
[21] T. Pavloudis, M. Zervos, P. Komninou, J. Kioseoglou, Ab-initio electronic structure calculations and properties of [SixSn1−x]3N4 ternary nitrides, Thin Solid Films 613 (2016) 43–47 https://doi.org/10.1016/j.tsf.2015.09.072.
[22] T.D. Boyko, E. Bailey, A. Moewes, P.F. McMillan, Class of tunable wide band gap semiconductors γ-(GexSi1-x)3N4, Phys. Rev. B 81 (2010) 155207 https://doi.org/10.1103/PhysRevB.81.155207.
[23] J.N. Hart, N.L. Allan, F. Claeyssens, Ternary silicon germanium nitrides: a class of tunable band gap materials, Phys. Rev. B 84 (2011) 245209 https://doi.org/10.1103/PhysRevB.84.245209.
[24] Y.-.X. Han, C.-.L. Yang, L.-.Z. Wang, M.-.S. Wang, X.-.G. Ma, Novel optical properties of γ-Si_3N_4 with B dopant, Mater. Chem. Phys. 161 (2015) 170–174 https://doi.org/10.1016/j.matchemphys.2015.05.032.
[25] Y.-.X. Han, C.-.L. Yang, K.-.L. Xiao, L.-.Z. Wang, M.-.S. Wang, X.-.G. Ma, Energy gap tuning and optical properties of γ-Si_3N_4 doped with Fe, Co and Ni, Mater. Sci. Semicond. Process. 27 (2014) 474–481 https://doi.org/10.1016/j.mssp.2014.07.019.
[26] Y. Zhang, X. Zhao, X. Cheng, Y. Mu, Density functional study on electronic properties of P-doped spinel silicon carbon nitride, J. Solid State Chem. 181 (2008) 2113–2116 https://doi.org/10.1016/j.jssc.2007.11.017.
[27] F. Oba, K. Tatsumi, H. Adachi, I. Tanaka, n- and p-type dopants for cubic silicon nitride, Appl. Phys. Lett. 78 (2001) 1577–1579 https://doi.org/10.1063/1.1354667.
[28] F. Oba, K. Tatsumi, I. Tanaka, H. Adachi, Effective doping in cubic Si_3N_4 and Ge_3N_4: a first-principles study, J. Am. Ceram. Soc. 85 (2002) 97–100 https://doi.org/10.1111/j.1151-2916.2002.tb00046.x.
[29] Y.C. Ding, A.P. Xiang, J. Luo, X.J. He, Q. Cai, X.F. Hu, First-principles study electronic and optical properties of p-type Al-doped γ-Si_3N_4, Physica B 405 (2010) 828–833 https://doi.org/10.1016/j.physb.2009.07.119.
[30] Y. Zhang, M. Antonietti, Photocurrent generation by polymeric carbon nitride solids: an initial step towards a novel photovoltaic system, Chem. Asian J. 5 (2010) 1307–1311 https://doi.org/10.1002/asia.200900685.
[31] J. Wang, H. Chen, S.-.H. Wei, W.-.J. Yin, Materials design of solar cell absorbers beyond Perovskites and conventional semiconductors via combining tetrahedral and octahedral coordination, Adv. Mater. 31 (2019) 1806593 https://doi.org/10.1002/adma.201806593.
[32] A. Bikowski, S. Siol, J. G, A. Holder, J.S. Mangum, B. Gorman, W. Tumas, S. Lany, A. Zakutayed, Design of metastable tin titanium nitride semiconductor alloys, Chem. Mater. 29 (2017) 6511–6517 2017/08/08 2017https://doi:, doi:10.1021/acs.chemmater.7b02122.
[33] S. Rühle, Tabulated values of the Shockley-Queisser limit for single junction solar cells, Sol. Energy 130 (2016) 139–147 http://dx.doi.org/10.1016/j.solener.2016.02.015.
[34] A. Zakutayev, Design of nitride semiconductors for solar energy conversion, J. Mater. Chem. A 4 (2016) 6742–6754 https://doi.org/10.1039/C5TA09446A.
[35] A. Luque, A. Martí, Increasing the efficiency of ideal solar cells by photon induced transitions at intermediate levels, Phys. Rev. Lett. 78 (1997) 5014–5017 https://doi.org/10.1103/PhysRevLett.78.5014.
[36] A. Luque, A. Marti, Photovoltaics: towards the intermediate band, Nat. Photon. 5 (2011) 137–138, doi:10.1038/nphoton.2011.22.
[37] A. Luque, A. Marti, C. Stanley, Understanding intermediate-band solar cells, Nat. Photon. 6 (2012) 146–152 https://doi.org/10.1038/nphoton.2012.1.
[38] P. Palacios, J.J. Fernández, K. Sánchez, J.C. Conesa, P. Wahnón, First-principles investigation of isolated band formation in half-metallic TixGa1-xP (x = 0.3125-0.25), Phys. Rev. B 73 (2006) 085206 https://doi.org/10.1103/PhysRevB.73.085206.
[39] C. Tablero, P. Palacios, J.J. Fernández, P. Wahnón, Properties of intermediate band materials, Sol. Energy Mater. Sol. Cells 87 (2005) 323–331 https://doi.org/10.1016/j.solmat.2004.06.016.
[40] P. Palacios, K. Sánchez, J.C. Conesa, P. Wahnón, First principles calculation of isolated intermediate bands formation in a transition metal-doped chalcopyrite-type semiconductor, Phys. Status Solidi A 203 (2006) 1395–1401 https://doi.org/10.1002/pssa.200566179.
[41] P. Palacios, K. Sánchez, J.C. Conesa, J.J. Fernández, P. Wahnón, Theoretical modelling of intermediate band solar cell materials based on metal-doped chalcopyrite compounds, Thin Solid Films 515 (2007) 6280–6284 http://dx.doi.org/10.1016/j.tsf.2006.12.170.
[42] I. Aguilera, P. Palacios, P. Wahnón, Optical properties of chalcopyrite-type intermediate transition metal band materials from first principles, Thin Solid Films 516 (2008) 7055–7059 https://doi.org/10.1016/j.tsf.2007.12.085.
[43] R. Lucena, I. Aguilera, P. Palacios, P. Wahnón, J.C. Conesa, Synthesis and spectral properties of nanocrystalline V-substituted In_2S_3, a novel material for more efficient use of solar radiation, Chem. Mater. 20 (2008) 5125–5127 https://doi.org/10.1021/cm801128b.
[44] P. Wahnón, J.C. Conesa, P. Palacios, R. Lucena, I. Aguilera, Y. Seminovski, F. Fresno, V-doped SnS_2: a new intermediate band material for a better use of the solar spectrum, Phys. Chem. Chem. Phys. 13 (2011) 20401–20407 https://doi.org/10.1039/C1CP22664A.
[45] R. Lucena, J.C. Conesa, I. Aguilera, P. Palacios, P. Wahnon, V-substituted In2S3: an intermediate band material with photocatalytic activity in the whole visible light range, J. Mater. Chem. A 2 (2014) 8236–8245 https://doi.org/10.1039/C4TA00513A.
[46] Y. Seminóvski, P. Palacios, J.C. Conesa, P. Wahnón, Thermodynamics of zinc insertion in CuGaS2:ti, used as a modulator agent in an intermediate-band photovoltaic material, Comput. Theor. Chem. 975 (2011) 134–137 http://dx.doi.org/10.1016/j.comptc.2010.12.018.
[47] Y. Seminóvski, P. Palacios, P. Wahnón, Intermediate band position modulated by Zn addition in Ti doped $CuGaS_2$, Thin Solid Films 519 (2011) 7517–7752 https://doi.org/10.1016/j.tsf.2010.12.136.
[48] Y. Seminovski, P. Palacios, P. Wahnón, Obtaining an intermediate band photovoltaic material through the Bi insertion in CdTe, Sol. Energy Mater. Sol. Cells 114 (2013) 99–103 https://doi.org/10.1016/j.solmat.2013.03.002.
[49] Y. Seminovski, P. Palacios, P. Wahnón, Analysis of SnS_2 hyperdoped with V proposed as efficient absorber material, J. Phys. 26 (2014) 395501 https://doi.org/10.1088/0953-8984/26/39/395501.
[50] J.E. Castellanos Águila, P. Palacios, J.C. Conesa, J. Arriaga, P. Wahnón, Theoretical band alignment in an intermediate band chalcopyrite based material, Appl. Surf. Sci. 24 (2017) 132–136 https://doi.org/10.1016/j.apsusc.2016.12.237.
[51] P. Palacios, I. Aguilera, P. Wahnón, J.C. Conesa, Thermodynamics of the Formation of Ti- and Cr-doped $CuGaS_2$ Intermediate-band Photovoltaic Materials, J. Phys. Chem. C 112 (2008) 9525–9529 https://doi.org/10.1021/jp0774185.
[52] K. Sánchez, I. Aguilera, P. Palacios, P. Wahnón, Assessment through first-principles calculations of an intermediate-band photovoltaic material based on Ti-implanted silicon: interstitial *versus* substitutional origin, Phys. Rev. B 79 (2009) 165203 https://doi.org/10.1103/PhysRevB.79.165203.
[53] K. Sánchez, I. Aguilera, P. Palacios, P. Wahnón, Formation of a reliable intermediate band in Si heavily coimplanted with chalcogens (S, Se, Te) and group III elements (B, Al), Phys. Rev. B 82 (2010) 165201 https://doi.org/10.1103/PhysRevB.82.165201.
[54] I. Aguilera, P. Palacios, P. Wahnón, Understanding Ti intermediate-band formation in partially inverse thiospinel $MgIn_2S_4$ through many-body approaches, Phys. Rev. B 84 (2011) 115106 https://doi.org/, doi:10.1103/PhysRevB.84.115106.
[55] G. García, M. Casanova-Páez, P. Palacios, E. Menéndez-Proupin, P. Wahnón, First principle study of V-implantation in highly-doped silicon materials, Comput. Mater. Sci. 136 (2017) 207–215 https://doi.org/10.1016/j.commatsci.2017.05.005.
[56] E. Garcia-Hemme, G. García, P. Palacios, D. Montero, R. García-Hernansanz, G. González-Diaz, P. Wahnón, Vanadium supersaturated silicon system: a theoretical and experimental approach, J. Phys. D (2017).
[57] G. García, P. Palacios, E. Menéndez-Proupin, A.L. Montero-Alejo, J.C. Conesa, P. Wahnón, Influence of chromium hyperdoping on the electronic structure of H3NH3PbI3 perovskite: a first-principles insight, Sci. Rep. (2018) 2511.
[58] P. Palacios, P. Wahnón, C. Tablero, Ab initio phonon dispersion calculations for TixGanAsm and TixGanPm compounds, Comput. Mater. Sci. (2005) 118–124.
[59] P. Palacios, P. Wahnón, S. Pizzinato, J.C. Conesa, Energetics of formation of TiGa3As4 and TiGa3P4 intermediate band materials, J. Chem. Phys. (2006).
[60] K. Hu, d. Wang, W. Zhao, Y. Gu, K. bu, J. Pab, P. Qin, X. Zhang, F. Huang, Intermediate band material of titanium-doped tin disulfide for wide spectrum solar absorption, Inorg. Chem. (2018) 3956–3962.
[61] P. Palacios, I. Aguilera, K. Sánchez, J.C. Conesa, P. Wahnón, Transition-metal-substituted indium thiospinels as novel intermediateband materials: prediction and understanding of their electronic properties, Phys. Rev. Lett. (2018).
[62] P. Palacios, K. Sánchez, P. Wahnón, J.C. Conesa, Characterization by ab initio calculations of an intermediate band material based on chalcopyrite semiconductors substituted by several transition metals, J. Sol. Energy Eng. (2006) 314–318.
[63] I. Aguilera, P. Palacios, P. Wahnón, Enhancement of optical absorption in Ga-chalcopyrite-based intermediate-band materials for high efficiency solar cells, Sol. Energy Mater. Sol. Cells (2010) 1903–1906.
[64] S. Ullah, H. Ullah, F. Bouhjar, M. Mollar, B. Marí, Synthesis of in-gap band CuGaS2:Cr absorbers and numerical assessment of their performance in solar cells, Sol. Energy Mater. Sol. Cells (2018) 322–327.
[65] A. Luque, A. Martí, E. Antolín, C. Tablero, Intermediate bands *versus* levels in non-radiative recombination, Physica B (2006) 320–327.
[66] P.E. Blöchl, Projector augmentedwave method Phys. Rev. B (1994) 17953–17979.
[67] G. Kresse, D. Joubert, From ultrasoft pseudopotentials to the projector augmented-wave method, Phys. Rev. B (1999) 1758–1775.
[68] G. Kresse, J. Hafner, Ab initio molecular dynamics for liquid metals, Phys. Rev. B (1993) 558–561.
[69] G. Kresse, J. Furthmüller, Efficient iterative schemes for ab initio total-energy calculations using a plane-wave basis set, Phys. Rev. B 54 (1996) 11169–11186, doi:10.1103/PhysRevB.54.11169.
[70] J.P. Perdew, K.B. Ernzerhof, Generalized gradient approximation made simple, Phys. Rev. Lett. (1996) 3865.
[71] M.K.Y. Chan, G. Ceder, Efficient band gap prediction for solids, Phys. Rev. Lett. (2010).
[72] L. Hedin, New method for calculating the one-particle green's function with application to the electron-gas problem, Phys. Rev. (1965) A796–A823.
[73] C. Faber, P. Boulanger, I. Duchemin, C. Attaccalite, X. Blase, Many-body Green's function GW and Bethe-Salpeter study of the optical excitations in a paradigmatic model dipeptide, J. Chem. Phys. (2013).

[74] S. Albrecht, L. Reining, R. Del Sole, G. Onida, Ab initio calculation of excitonic effects in the optical spectra of semiconductors, Phys. Rev. Lett. (1998) 4510–4513.
[75] M. Rohlfing, S.G. Louie, Electron-Hole Excitations in Semiconductors and Insulators, Phys. Rev. Lett. (1998) 2312–2315.
[76] R. Grau-Crespo, S. Hamad, C.R.A. Catlow, N.H. de Leeuw, Symmetry-adapted configurational modelling of fractional site occupancy in solids, J. Phys. (2007).
[77] D.W. Smith, Inorganic Substances: a Prelude to the Study of Descriptive Inorganic Chemistry (Cambridge Texts in Chemistry and Biochemistry) Cambridge University Press Cambridge (1990).
[78] M.P. Shemkunas, G.H. Wolf, K. Leinenweber, W.T. Petuskey, Rapid synthesis of crystalline spinel tin nitride by a solid-state metathesis reaction, J. Am. Ceram. Soc. (2002) 101–104.
[79] W. Sun, A. Holder, B. Orvañanos, E. Arca, A. Zakutayed, S. Lany, G. Ceder, Thermodynamic routes to novel metastable nitrogen-rich nitrides, Chem. Mater. (2017) 6936–6946.
[80] W. Sun, C.J. Bartel, E. Arca, S.R. Bauers, B. Matthews, B. Orvañanos, B.-.R. Chen, M.F. Toney, L.T. Schelhas, W. Tumas, J. Tate, Z. Zakutaved, S. Lany, A.M. Holder, G. Ceder, A map of the inorganic ternary metal nitrides, Nat. Mater. (2019) 732–739.
[81] V. Stevanović, S. Lany, X. Zhang, A. Zunger, Correcting density functional theory for accurate predictions of compound enthalpies of formation: fitted elemental-phase reference energies, Phys. Rev. B (2012).
[82] A.M. Deml, R. O'Hayre, C. Wolverton, V. Stevanović, Predicting density functional theory total energies and enthalpies of formation of metal-nonmetal compounds by linear regression, Phys. Rev. B (2016).
[83] M.P. Shemkunas, W.T. Petuskey, A.V.G. Chizmeshya, K. Leinenweber, G.H. Wolf, Hardness elasticity, fracture toughness of polycrystalline spinel germanium nitride and tin nitride, J. Mater. Res. (2004) 1392–1399.
[84] T.D. Boyko, A. Moewes, The hardness of group 14 spinel nitrides revisited, J. Ceram. Soc. Jpn. (2016) 1063–1066.
[85] A. Šimůnek, J. Vackář, Hardness of covalent and ionic crystals: first-principle calculations, Phys. Rev. Lett. (2006).
[86] F.A. Cotton, A millennial overview of transition metal chemistry, J. Chem. Soc. Dalton Trans. (2000) 1961–1968.
[87] F.A. Cotton, I - Ligand field theory, J. Chem. Educ. (1964) 466.
[88] P. Zimmermann, N. Bouldi, M.O.J. y. Hunault, M. Sikora, J.M. Ablett, J.-P. Rueff, B. Lebert, P. Sainctavit, F.M.F. de Groot, A. Juhin, 1s2p resonant inelastic X-ray scattering magnetic circular Dichroism as a probe for the local and non-local orbitals in CrO 2, J. Electron Spectrosc. Relat. Phenom. (2018) 74–87.
[89] A. Krishna, J.J. Krich, Increasing efficiency in intermediate band solar cells with overlapping absorptions, J. Opt (2016).